Concerted Proton-Electron Transfer Minimizes Substituent Effects on Adsorbed Phthalocyanine Electrocatalysis

Vennela Mannava[1], Logan E. Smith[2], Joel G. Gardner[1], Sharon Hammes-Schiffer[2], and Yogesh Surendranath[1]*

[1]Department of Chemistry, Massachusetts Institute of Technology, Cambridge, Massachusetts 02139, United States

[2]Department of Chemistry, Princeton University, Princeton, New Jersey 08544, United States

*Corresponding author: yogi@mit.edu

Abstract:

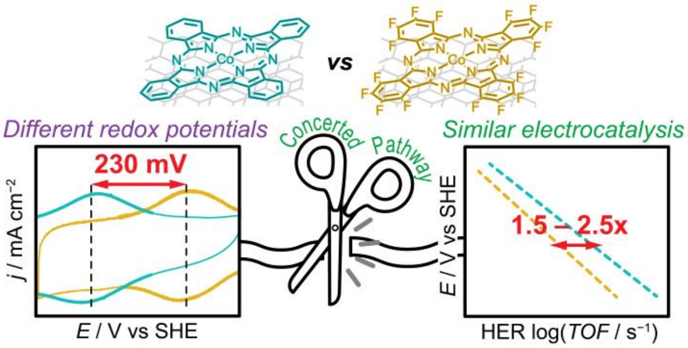

Molecularly modified electrodes (MMEs) are potent electrocatalysts, but few principles exist for their rational design. Electrocatalysis by soluble molecules depends strongly on substituents that tune the catalyst redox potential ($E_{1/2}$), but it is unclear if this parameter similarly impacts MME catalysis. Herein, we employ the hydrogen evolution reaction (HER) as a test case for comparing carbon-adsorbed cobalt phthalocyanine (CoPc/C) and cobalt hexadecafluoro-phthalocyanine (CoFPc/C). By correlating HER activity and voltammetric data to total Co surface concentration across a wide range of catalyst loadings, we find that only 5-25% of adsorbed Co sites contribute to the Co(II/I) redox wave, and that this subpopulation poorly correlates with catalytic activity. Instead, in the low-loading limit, catalytic activity correlates linearly with the majority Co(II/I)-silent Co population, revealing per-site turnover frequency (TOF) values for HER. Despite a 230 mV difference in Co(II/I) redox potentials, CoPc/C and CoFPc/C display TOF values differing by less than a factor of 3 when compared over a wide potential range. Mechanistic studies point to an inner-sphere concerted proton-electron transfer (CPET) step as rate-determining, suggesting that

the Co–H bond dissociation free energy (BDFE) rather than the Co(II/I) $E_{1/2}$ is thermodynamically relevant. Computational studies indicate that the fluoro-substituents lead to compensatory changes in Co(II/I) $E_{1/2}$ and Co(I) basicity, leaving the Co–H BDFE largely unchanged between CoPc and CoFPc and thereby manifesting in similar catalytic rates. These results highlight the limited effect of $E_{1/2}$-tuning on MME catalytic activity and motivate the development of methods to directly alter active site–substrate BDFE.

Introduction

Molecularly modified electrodes (MMEs) are a valuable class of materials for the study and development of complex electrocatalytic processes.[1–8] They consist of a molecular active site covalently attached or non-specifically adsorbed to an inert electrode support in order to create a heterogeneous electrocatalyst. The precise chemical environment of the molecular active site and its interactions with the electrode can lead to distinct reactivity relative to either individual component. For example, cobalt phthalocyanines adsorbed on carbon nanotube-based electrodes have demonstrated CO_2 electroreduction to methanol, a unique selectivity unattainable with independent molecular or carbon electrocatalysts.[9–12] Thus, uncovering the mechanistic impacts of molecule-electrode interactions is a prerequisite for the rational design of new MMEs tailor-made for (electro)catalytic applications.

One characteristic parameter often considered in both MME and homogeneous molecular electrocatalysis is the molecular redox potential, $E_{1/2}$, of the redox couple proposed to be involved in the catalytic mechanism. In this paper, we use molecular $E_{1/2}$ to denote the equilibrium potential of an electron transfer (ET) process uncoupled to any proton transfer (PT) process. For typical homogeneous molecular electrocatalysis, the overall reaction is mediated by outer-sphere ET to reduce (or oxidize) the catalyst, followed by substrate activation by the reduced (or oxidized) catalyst in solution. **Figure 1a** depicts a simplified molecular electrocatalytic cycle for proton activation to generate hydrogen. Since this catalytic sequence is mediated via a discrete reduced intermediate, the $E_{1/2}$ for the mediating redox process is a central descriptor of electrocatalytic activity.[13–19] Indeed, the molecular $E_{1/2}$ establishes the potential range over which catalysis onsets and typically correlates with the driving force for the subsequent substrate activation step. Consequently, the molecular $E_{1/2}$ is a prime target for modification to alter catalytic activity. While de novo design of a molecule with a particular $E_{1/2}$ is challenging, synthetic addition of electron-donating or -withdrawing groups is a facile technique to shift $E_{1/2}$ in a predictable fashion.[20–22] $E_{1/2}$ tuning has also been employed to diagnose mechanism in molecular electrocatalytic sequences, further reinforcing its importance.[17–19] As this discussion highlights, $E_{1/2}$ is a central parameter under consideration in the design and optimization of homogeneous molecular electrocatalysts.

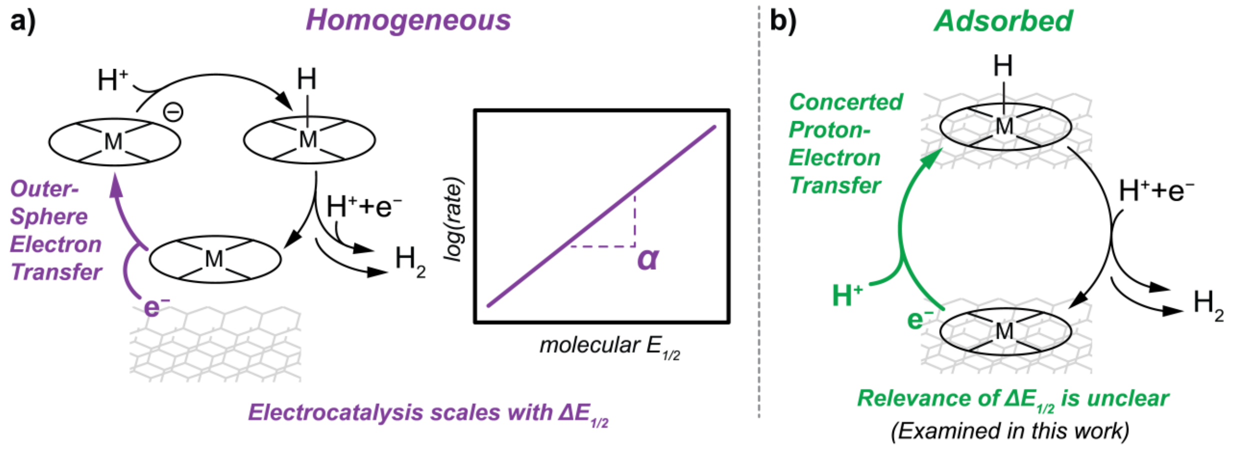

Figure 1. Simplified mechanistic pathways for hydrogen evolution electrocatalysis at a homogenous vs. surface-adsorbed molecule. **a)** Homogenous molecule mediates the conversion of 2 H^+ and 2 e^- to H_2 through a stepwise pathway involving outer-sphere electron transfer followed by a chemical step for proton activation. The plot depicts that homogeneous electrocatalytic turnover frequency (TOF) scales with the molecular redox potential ($E_{1/2}$) by a factor α. **b)** Adsorbed molecule catalyzes the conversion of 2 H^+ and 2 e^- to H_2 through concerted proton-electron transfer to form a surface M–H intermediate.

Despite the established primacy of the molecular $E_{1/2}$ in homogeneous molecular electrocatalysis, it remains unclear if this parameter is equally important for MME electrocatalysis. Our previous work evinces that concerted pathways, rather than stepwise, redox-mediated, ones are in play for certain MME reactions.[23,24] For example, we have found that upon strong adsorption of a carbon-tethered cobalt porphyrin to the carbon surface, hydrogen evolution reaction (HER) catalysis proceeds through concerted proton-electron transfer (CPET) steps (**Figure 1b**).[25–27] Specifically, our prior studies have shown that molecules strongly adsorbed to graphitic carbon can reside within the electrochemical double layer (EDL), leading to minimal electrostatic potential drop between the surface and the adsorbed molecule. Consequently, applying a potential to the electrode does not generate a driving force for transferring electrons from the band states of the carbon to the orbitals of the adsorbed molecules, and so these adsorbed molecules do not undergo outer-sphere ET. Instead, experimental data and computational models of an adsorbed Co porphyrin support a picture in which protons cross the EDL to bind directly to the Co site, inducing concerted electron localization from the carbon to form the Co–H bond.[24–26] Since this concerted inner-sphere mechanism bypasses discrete redox intermediates, the relevance of the molecular $E_{1/2}$ as a thermodynamic descriptor of reactivity becomes unclear.

The ambiguity about the role and importance of $E_{1/2}$ for these MMEs is compounded by the connection between ET and PT thermochemistry observed in proton-coupled electron transfer (PCET) sequences for many homogeneous molecules. Substituents altering ET or PT thermochemistry can alter the other in a compensatory way such that overall PCET thermochemistry is relatively unchanged.[28–30] These compensation phenomena are dependent on factors such as substituent position and extent of proton and electron localization.[31–33] Thus, it is unclear whether substituents that change $E_{1/2}$ also change the overall PCET thermochemistry in MME systems and whether there is any effect on electrocatalytic activity.

Despite the emerging understanding of the critical mechanistic distinction between outer-sphere and inner-sphere pathways for MMEs, redox features observed on MMEs and the molecular $E_{1/2}$ values extracted from those features are often invoked in analysis of MME electrocatalysis. One reason could be that $E_{1/2}$ is an easily accessible parameter for MMEs, particularly compared to more obscured variables such as active site microenvironment.[34–38] This has led, for example, to the use of $E_{1/2}$ values in structure-function correlations for O_2 electroreduction by carbon-adsorbed metal macrocycles,[39,40] or in the assignment of catalytic active states for CO_2 electroreduction by carbon-adsorbed cobalt macrocycles.[12,41–43] Indeed, it is common practice in MME electrocatalysis, particularly for carbon-adsorbed cobalt phthalocyanines, to use the integration of the Co(II/I) redox wave to quantify electroactive sites.[44,45] This follows from the assumption that those sites giving rise to the Co(II/I) voltammetric signal comprise the entire catalytically active population. However, our previous work has shown that catalytically active molecules strongly adsorbed within the EDL do not give rise to outer-sphere ET redox waves.[24–26] Thus, it remains unclear whether the outer-sphere Co(II/I) redox-active sites are the catalytically active species, and what contribution to catalytic activity emerges from outer-sphere Co(II/I)-silent sites. The presence of these multiple populations emerges from the tendency of planar macrocycles such as phthalocyanines to self-aggregate, which has been demonstrated to affect both the redox and catalytic activity.[44,46,47] While the extent of aggregation can be modified via changes to substituents, solvent, and/or support, the ensuing changes to redox and catalytic activity are always convoluted with each other.[10,48,49] All of these ambiguities motivate the development of improved methods for quantifying both outer-sphere ET redox-active and inactive subpopulations in MMEs across a range of loadings in order to parse their relative contributions to catalytic activity and to isolate reliable per-site turnover frequency (TOF) values for comparison between molecules.

Herein, we compare the kinetics and mechanism of aqueous HER catalysis by two carbon-adsorbed cobalt phthalocyanines with distinct electron-richness in order to address two questions: (1) is molecular $E_{1/2}$ a good descriptor of electrocatalysis by carbon-adsorbed cobalt phthalocyanines; and (2) why or why not? We selected HER as an ideal test reaction because of the limited mechanistic possibilities for combining two protons and two electrons, permitting clearer discrimination between redox-mediated and concerted pathways. We selected carbon-adsorbed cobalt phthalocyanines because they are a common subclass of MMEs that are known to be competent for HER electrocatalysis, with the Co(II/I) redox couple in particular often invoked to be catalytically relevant.[4,50–54] Based on these considerations, we compared HER catalysis by carbon-adsorbed cobalt phthalocyanine (CoPc/C) and carbon-adsorbed cobalt hexadecafluoro-phthalocyanine (CoFPc/C) to assess the role of molecular $E_{1/2}$ in catalytic activity.

In order to compare HER activity quantitatively across these two non-specifically adsorbed molecules, we first develop a kinetically validated method to estimate active site populations. Our method reveals the presence of two molecular populations on the surface: a majority of outer-sphere Co(II/I) redox-silent molecular sites that correlate with HER activity, and a small minority of outer-sphere Co(II/I) redox-active sites that do not correlate with HER activity. Thus, we use total Co loading rather than Co(II/I) redox integration to estimate active site counts and to generate lower-limit site-normalized HER TOF values across a range of applied potentials. These analyses reveal that CoPc/C and CoFPc/C display similar activity with less than a 3-fold difference in rate, despite a 230 mV difference in Co(II/I) $E_{1/2}$ values. Mechanistic studies support that both systems proceed through an inner-sphere CPET-limited pathway, for which Co–H bond dissociation free energy (BDFE) rather than Co(II/I) $E_{1/2}$ is expected to be thermodynamically relevant. Computational studies indicate that the large $\Delta E_{1/2}$ between CoPc and CoFPc is compensated for by an opposing change in the basicity of the reduced catalyst, leading to similar Co–H BDFE values and correspondingly similar HER activity. Based on these findings, we conclude that the binding affinity for the key intermediate is a better descriptor of catalytic activity by surface-adsorbed molecules than the molecular $E_{1/2}$, and that classical $E_{1/2}$ tuning efforts may not improve MME catalysis because they generally do not alter the BDFE of reaction intermediates. Corroborating the growing appreciation of substrate binding strengths in the MME literature,[39,43,55,56] our results promote BDFE as a more effective target than $E_{1/2}$ for molecular design efforts in MME electrocatalysis.

Results and Discussion

CoPc/C and CoFPc/C Display Distinct Co(II/I) Redox Potentials

In order to understand the relevance of molecular $E_{1/2}$ to HER catalysis, we first sought to quantify the Co(II/I) thermochemistry for CoPc and CoFPc. The extreme aqueous insolubility and surface affinity of CoPc and CoFPc impeded $E_{1/2}$ quantification for the soluble molecules. Instead, we extracted Co(II/I) $E_{1/2}$ values from outer-sphere redox-active populations within CoPc/C and CoFPc/C MME films. Each MME film was a composite of the cobalt phthalocyanine, carbon black, and a polymeric binder supported on a glassy carbon rotating disk electrode (RDE). First, we prepared an ink of 2.5 mg Vulcan XC-72R carbon black powder and varying amounts (0.03-1.3 mg) of the molecular catalyst in 0.9 mL *N*,*N*-dimethylformamide (DMF) with 0.1 mL of 5 wt.% Nafion solution. This ink was sonicated until the liquid was visibly indistinguishable from the well-dispersed solid. 10 μL of this ink suspension were dropcast onto a 5 mm glassy carbon rotating disk electrode (RDE). The films were dried in an oven at 80 °C for at least 30 minutes (see SI for additional details). This procedure furnishes films which display minimal film-to-film variations across our analyses, enabling extraction of reliable electrochemical parameters.

We examined the MMEs generated by the above procedure by cyclic voltammetry (CV) in pH 13 electrolyte (0.1 M NaOH) under Ar at 2000 R.P.M. rotation rate. CoPc/C displays a reversible couple assigned to the Co(II/I) redox process at −0.40 V vs. SHE (all potentials are reported vs. SHE unless otherwise noted) (**Figure 2a**). This $E_{1/2}$ is independent of scan rate (**Figure S3**), electrolyte pH (**Figure S4**), and catalyst loading (**Figure S5**), and is thus assigned to a simple proton-uncoupled outer-sphere ET process. CoFPc/C displays a similarly pH-independent reversible couple assigned to the Co(II/I) redox process at −0.12 V (**Figure S6**). For both catalyst films, this signal is unchanged by cycling 9 times or by conducting electrolysis for 20 min at −1.23

V vs. SHE (**Figure S7**). However, there is a marked scan rate and CoFPc loading dependence to the reversibility of the wave and its $E_{1/2}$ value for CoFPc/C (**Figures S8-10**). Based on the reversibility at scan rates of 100 mV s^{-1} and above, and presuming that surface effects are less salient for higher CoFPc loading films, where many more molecules may be adsorbed to each other rather than the surface (see SI Supplemental Note on CoFPc/C Co(II/I) Redox for full details), we use the $E_{1/2}$ of −0.17 V determined at 100 mV s^{-1} in the 37 nmol cm^{-2} CoFPc loading films to define the Co(II/I) redox potential for CoFPc/C (**Figure 2a**). This defines an overall $\Delta E_{1/2}$ of 230 mV, or 5.3 kcal mol^{-1}, indicating a large energetic difference in the Co(II/I) thermochemistry of CoPc/C versus CoFPc/C. This shift is attributed to the electron-withdrawing character of the 16 fluoro-substituents which leads to a more electron-poor Co center in CoFPc relative to CoPc. We do not observe any more negative redox process for either MME film prior to catalytic onset in pH 13 conditions, although we might expect such processes to have a similar delta based on literature reports.[57–59] Ultimately, the observed redox features evince the distinct Co(II/I) redox thermochemistry of CoPc/C and CoFPc/C.

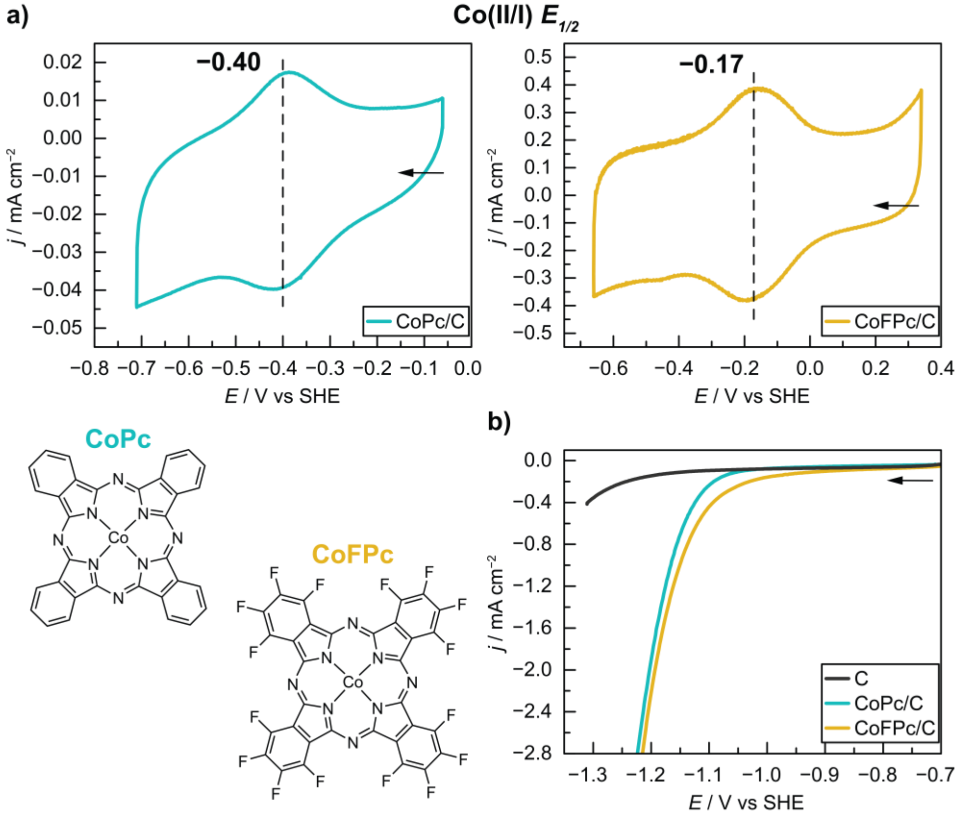

Figure 2. Depictions of molecular CoPc and CoFPc along with Co(II/I) redox and HER catalysis data. **a)**

Cyclic voltammograms of CoPc/C and CoFPc/C recorded at 5 and 100 mV s^{-1}, respectively. Nominal catalyst loadings are 80 and 42 nmol cm^{-2}, respectively, based on geometric electrode surface area. **b)** Linear sweep voltammograms of C, CoPc/C, and CoFPc/C recorded at 5 mV s^{-1}. Nominal catalyst loadings are 0, 36, and 42 nmol cm^{-2}, respectively. Each arrow indicates voltammetric scan direction. All data were measured in 0.1 M NaOH under Ar at 2000 R.P.M.

Catalyst Loading Dependence Enables HER Turnover Frequency Quantification

We next investigated the ability of each MME system to conduct HER electrocatalysis. All experiments were conducted in pH 13 electrolyte (0.1 M NaOH) under Ar at 2000 R.P.M. rotation rate. In this pH condition, the proton donor is water and thus, its concentration remains constant. The experiments were conducted at a high rotation rate as an added precaution to mitigate the buildup of any local gradients in OH^{-}. An unmodified carbon black film shows no substantial HER current until approximately −1.25 V, where it reaches −0.2 mA cm^{-2} (**Figure 2b**). In contrast, CoPc/C and CoFPc/C films show HER onset of −0.2 mA cm^{-2} at −1.09 and −1.03 V, respectively (**Figure 2b**). CoPc/C and CoFPc/C catalyze HER above the C background and a redox-inert ZnPc/C film in steady-state measurements as well (**Figure S11**). The substantial enhancement in HER above the C background is indicative of catalysis by the adsorbed CoPc or CoFPc species.

To minimize convolution from Co nanoparticulate decomposition products and diagnose their role, if any, we took the following precautions. To avoid reductive decomposition, all steady-state HER experiments were conducted at relatively mild potentials, the most extreme being −1.23 V at which point steady state current densities are less than −2.8 mA cm^{-2}. The current transients also imply negligible convolution from Co nanoparticles. When held at −1.23 V, HER currents by a representative 4.1 nmol cm^{-2} CoPc/C film decay from −1.04 to −0.91 mA cm^{-2} over 15 min of electrolysis (**Figure S12**). Likewise, when held at −1.23 V, HER currents by a representative 4.9 nmol cm^{-2} CoFPc/C film decay from −0.96 to −0.91 mA cm^{-2} over 15 min of electrolysis (**Figure S12**). In contrast, an analogous film prepared with 7.2 nmol cm^{-2} $CoCl_2$/C instead shows activation under the same conditions and applied potential, with HER currents rising from −0.50 to −0.65 mA cm^{-2} over 15 min of electrolysis (**Figure S12**). These contrasting temporal profiles suggest that the HER current observed for CoPc/C or CoFPc/C is not substantially convoluted by HER activity of Co nanoparticles over the timescale of our measurements. Taken together, the above results indicate that each molecular cobalt phthalocyanine displays intrinsic HER activity in each MME film.

In order to compare the HER activities for CoPc/C and CoFPc/C quantitatively as per-site TOF values, we first estimated the active Co population in each film. Due to the variety and complexity of molecular environments available for non-specifically adsorbed molecules, which can form various aggregated states on the surface, there exists a limited toolkit for active site counting. To avoid making assumptions about site identities, we employed a method for estimating active site counts based on the Madon-Boudart test, which assesses whether measured catalytic activity scales with catalyst loading.[60] For both CoPc/C and CoFPc/C systems, we varied the catalyst loading and recorded HER Tafel data (log-scale current density, log(j), versus applied potential, E) via a series of chronoamperometry experiments across varied applied potentials (**Figures S13-15**). Following Tafel data collection, we digested each film in acid and quantified the Co loading via inductively coupled plasma-mass spectrometry (ICP-MS) analysis (see SI for experimental details). Using the measured Co loading value, we calculated apparent TOF values on a per Co basis and constructed site-normalized Tafel plots of log(TOF) versus applied potential, E (**Figure 3**) (**Figures S14-15**) (see SI for additional details). For both MME systems, the lower loading films with 3.6 to 8.9 nmol cm^{-2} Co (**Figure 3** left, blue to green; right, yellow to brown) display apparent log(TOF) values that overlay within error of each other across the entire measured E range. In contrast, the higher loading films with 37 to 71 nmol cm^{-2} Co (**Figure 3** left, purple to lavender; right, red to pink) display suppressed apparent log(TOF) values. For example, for CoPc/C at −1.14 V, the lower loading films all display apparent TOF values of approximately 0.32 s^{-1}, whereas for the higher loading films apparent TOF values are depressed by a factor of 3-4 to 0.10 and 0.07 s^{-1}. Similarly, for CoFPc/C at −1.14 V, the lower loading films all display TOF values of approximately 0.15 s^{-1}, whereas for the higher loading films apparent TOF values are depressed by a factor of 2-3 to 0.09 and 0.04 s^{-1}. The attenuation in apparent TOF observed at higher loadings is indicative of ineffective catalyst utilization and, thus, only the lower loading data is reflective of the intrinsic TOF of the CoPc/C or CoFPc/C.

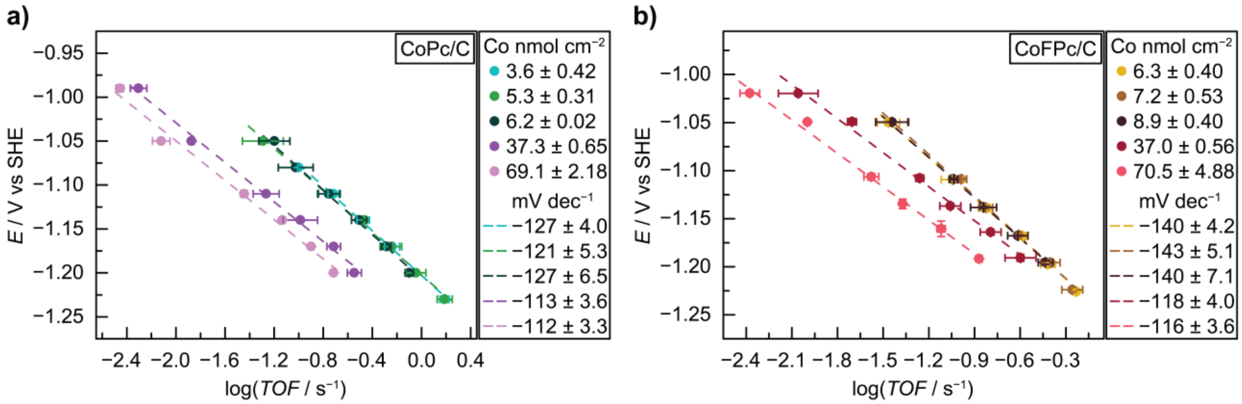

Figure 3. log(TOF) vs. *E* data from **a)** CoPc/C and **b)** CoFPc/C films across various catalyst loadings. The log(*j*) values were collected via a series of chronoamperometry experiments across varied applied potentials and then converted into log(TOF) using the ICP-MS measured total Co loading of each film. The points and error bars represent averages and standard deviations for triplicate films for each loading. The dashed lines represent linear fits of the unaveraged independent film data for each loading with the slopes and errors noted in the legend. All data were measured in 0.1 M NaOH under Ar at 2000 R.P.M.

We further analyzed the same CoPc/C and CoFPc/C films to better understand the dependence of HER activity on catalyst loading. The preceding trends can be visualized as plots of log(TOF) vs. log(*loading*), which reveal an invariance in apparent log(TOF) at lower loadings (3.6 to 8.9 nmol cm^{-2}) that is followed by a steep drop-off in apparent log(TOF) at higher loadings (37 to 71 nmol cm^{-2}) (**Figures S16-17**). The same data can also be replotted as log(*j*) vs. log(*loading*), which returns a reaction order in Co loading of approximately 1 for catalyst loadings up to 6.2 and 8.9 nmol cm^{-2} for CoPc/C and CoFPc/C, respectively, followed by a sharp transition in the Co loading order to approximately 0 (**Figures S18-19**). These data evince a transition after 6.2 and 8.9 nmol cm^{-2} catalyst loading for CoPc/C and CoFPc/C, respectively, above which the HER activity fails to scale fully with loading, indicative of the presence of a large proportion of inactive Co sites in the high loading films. Scanning electron microscopy-energy dispersive X-ray spectroscopy (SEM-EDS) imaging of a nominally 80 nmol cm^{-2} loading CoPc/C film reveals the presence of large CoPc crystals (**Figure S20a**), suggesting the presence of electrochemically inaccessible inactive sites. Large CoFPc crystals were also observed in SEM-EDS images of a nominally 77 nmol cm^{-2} loading CoFPc/C film (**Figure S20b**), while no crystal formations were detected in SEM images of lower loading films (4.5 nmol cm^{-2} CoPc/C; 8.3 nmol cm^{-2} CoFPc/C films) (**Figure S20c-d**). These imaging data are consistent with the observed drop-off in apparent TOF values and transition from 1st to 0th order dependence on Co loading. We note that the above analyses are not able to discern the presence of a loading-independent fraction of inactive sites, since that would also scale 1:1 with the active site population. As such any TOF we report based on ICP-MS is a lower-limit TOF as is commonly accepted in heterogenous catalysis.

This ICP-MS-based method is at odds with the more common practice for counting active sites in cobalt phthalocyanine MME systems, which uses integration of the Co(II/I) voltammetric wave. However, we observe in our conditions that the Co(II/I) wave integration is often between 5 and 15% of the total ICP-MS-measured Co loading, and never exceeds 25% (**Figures S21-22**). These Co sites quantified by integration of the Co(II/I) outer-sphere ET redox feature in pH 13 voltammetry are referred to as the "OSET-active" population, while the remainder of any Co sites in the film are referred to as the "OSET-silent" population. Previous work has shown that HER activity can arise from surface-bound catalyst sites that do not themselves give rise to an outer-sphere Co(II/I) CV response.[23,25] To probe whether OSET-active populations correlate with HER activity in our MME films, we converted the data from **Figure 3** into TOF values based on each film's OSET-active molecule loading rather than the total ICP-MS-measured Co loading (**Figures S23-24**). For both CoPc/C and CoFPc/C films, the log($TOF_{\textit{OSET-active}}$) values decrease with OSET-active molecule loading (**Figure S23b** and **S24b**), over the same total loading regime where the log(TOF) values based on ICP-MS are constant. The lack of a consistent per-site HER activity when using active site counts derived from the outer-sphere Co(II/I) redox signal suggests that the molecules giving rise to Co(II/I) voltammetric waves are not substantially contributing to the aggregate HER activity of the MME film. Put another way, the OSET-active population may catalyze HER, but the associated activity is undetectably low compared to the OSET-silent population in the potential window of our analysis. Based on this finding, we strongly favor the ICP-MS-based analysis methods over integration of the Co(II/I) voltammetric wave. We note that conversion of the data from **Figure 3** into "corrected" TOF values, where the OSET-active population was subtracted from the total ICP-MS-measured Co loading, returned the same data trends as **Figures S14-19** but with slightly higher absolute TOF values, as expected when subtracting a small subpopulation of Co sites (**Figures S25-26**). Since this correction method likely introduces further measurement errors into the active site count and results in no changes to our conclusions, we instead retain the rigorously lower-limit TOF values derived from ICP-MS measurement alone. Ultimately, the Tafel data coupled with ICP-MS-based Madon-Boudart analysis reveals a low catalyst loading regime in which total Co loading may be taken as a reasonable estimate of the active site count, since it results in invariant lower-limit log(TOF) values.

CoPc/C and CoFPc/C Display Similar HER Turnover Frequencies

With per-site HER TOF estimates in hand, we proceeded to quantitatively compare the two MME systems. All nine CoPc/C films and all nine CoFPc/C films within the validated lower-loading regimes were used to generate a global linear fit in log(TOF) vs. *E* for each MME system (**Figure 4**) (**Figure S27**). Since the lower-loading log(TOF) values all align, for each MME system there is no significant difference between those three fits in **Figure 3a** or **3b** and the corresponding fit accounting for all of the lower-loading films in **Figure 4**. Correspondingly, the global CoPc/C fit has a slope of −123 ± 3.1 mV dec^{-1} and the CoFPc/C fit has a slope of −141 ± 2.9 mV dec^{-1}. Overall, the CoPc/C and CoFPc/C HER activities are remarkably similar across this *E* range, especially at milder applied potentials where the data overlay within error. Due to the slight difference in Tafel slopes, the CoPc/C and CoFPc/C data diverge increasingly with more negative applied potentials. However, the largest difference is still only approximately 0.4 orders of magnitude, or a factor of 2.5, in TOF at −1.23 V. The similar activity between the two molecules is striking, given that electrocatalytic TOF is typically strongly correlated with the molecular $E_{1/2}$ for redox-mediated molecular systems. Indeed, despite the 230 mV difference in $E_{1/2}$ values, the two catalysts display a common rate at potentials that deviate by only 30 to 50 mV across the range of data collection. These data indicate that the molecular $E_{1/2}$ is not a good descriptor of relative HER activity for these carbon-adsorbed cobalt phthalocyanines.

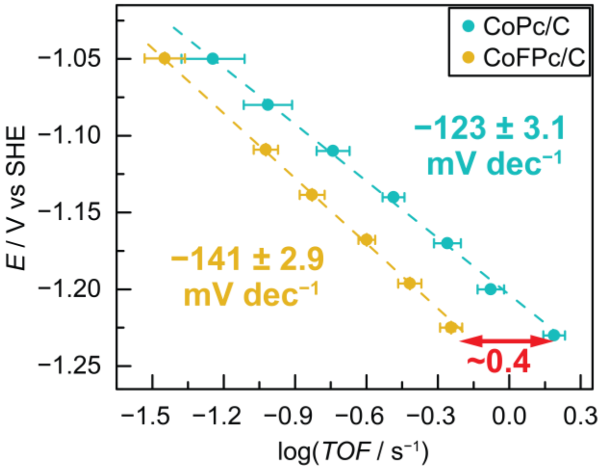

Figure 4. log(TOF) vs. *E* data from films with catalyst loadings in the regime displaying 1st order kinetics in catalyst loading (the 3 lower loadings in **Figure 3a** and **3b)**. The points and error bars show averages and standard deviations for all 9 films. The dashed lines represent linear fits of the unaveraged independent film data with the slopes and errors noted.

HER Mechanistic Data Are Consistent with a Concerted PCET Pathway

In order to uncover the reason that the large difference in molecular $E_{1/2}$ does not translate into substantial changes in HER activity by these carbon-adsorbed cobalt phthalocyanines, we sought to investigate the mechanism of catalysis in greater detail. First, we analyzed each Tafel slope. As shown in **Figure 4**, the HER Tafel slope is −123 ± 3.1 mV dec^{-1} for CoPc/C and −141 ± 2.9 mV dec^{-1} for CoFPc/C. To diagnose whether the Tafel data is influenced by internal transport artifacts we repeated the Tafel experiments with half-thickness films created by dropcasting half the typical amount of catalyst/carbon ink. Not only do these half-thickness films show no decrease of Tafel slope for either MME system, the log(TOF) values of these films, which also contained half the catalyst loading, returned the same per site TOF as the original dataset (**Figures S28-29**). This alignment suggests that internal transport artifacts are not substantially convoluting any of our low loading data and that the log(TOF) values represent activation-controlled kinetics. The observed Tafel slopes correspond to transfer coefficients for HER catalysis of 0.48 and 0.42, respectively. A transfer coefficient of approximately 0.5 for HER is suggestive of a single rate-determining charge transfer step and is at odds with mechanisms involving one or more quasi-equilibrated charge transfer steps, which would generally give rise to Tafel slopes of −59 mV dec^{-1} or lower in magnitude. Taken together, the foregoing analysis suggests that HER catalysis by both CoPc and CoFPc proceeds via a single, rate-determining charge transfer step.

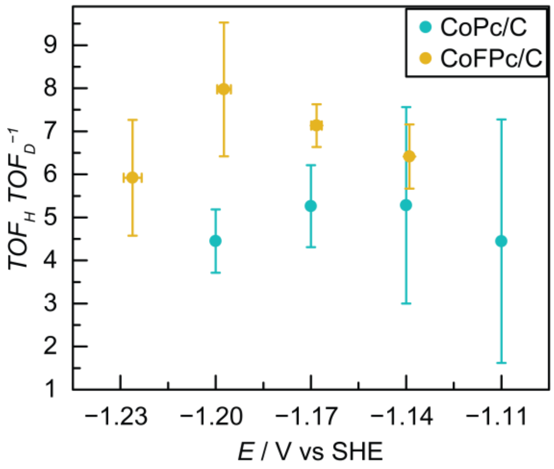

Figure 5. H/D KIE for CoPc/C and CoFPc/C derived from the TOF values at select *E* measured in 0.1 M NaOH in H_2O or D_2O under Ar at 2000 R.P.M. The TOF average and standard deviation for triplicate catalyst films in each electrolyte were then divided to generate the $\mathrm{TOF}_H\ \mathrm{TOF}_D^{-1}$ average and standard deviation plotted here.

To further examine the nature of the rate-determining step (RDS), we analyzed the H/D kinetic isotope effect (KIE). Comparison of HER in 0.1 M NaOH in H_2O and D_2O reveals an H/D KIE for CoPc/C of approximately 5 ± 2, and an H/D KIE for CoFPc/C of approximately 7 ± 1 (**Figure 5**) (see SI for additional details). High KIE values such as these are relatively common for inner-sphere concerted proton-electron transfer (CPET) steps involved in electrocatalysis.[61–63] The Tafel slopes are identical within error between H_2O and D_2O electrolytes, leading to roughly potential-independent KIE values across the catalytic range (**Figures S30-31**). The clear observation of a KIE above 1 for each MME system implicates a proton transfer (PT) in the RDS for HER catalyzed by CoPc/C or CoFPc/C. Together, the Tafel and H/D KIE data are consistent with concerted proton-electron transfer (CPET) as the RDS for HER by these MME systems. The Tafel slope values and the lack of any prefeature wave prior to catalytic onset support that the rate-determining CPET is the Volmer step of HER, which is the CPET step forming the putative Co–H intermediate. The foregoing kinetic data do not necessarily rule out rate-determining CPET to the Pc ligand (e.g., protonation at a bridgehead N atom) as an alternative mechanism. However, this pathway seems unlikely since the native polarity of an N–H intermediate inhibits its action as a hydride donor in the subsequent step of H_2 formation.[32] Additionally, experimental non-idealities prevented kinetic analyses in lower pH conditions, meaning a consistent mechanism across pH cannot be verified. If the CPET mechanism holds across pH, the first-order expectation is that the proton donor dependence is similar between CoPc/C and CoFPc/C, thus preserving the similarity in their HER activities. Regardless, speaking to the pH 13 data alone, the analyses support that CoPc/C and CoFPc/C catalyze HER via a common rate-determining CPET mechanism.

We next consider the outer-sphere or inner-sphere character of the rate-determining CPET step. Outer-sphere CPET involves electron tunneling across the EDL that is concerted with proton binding. The ability to perform outer-sphere CPET during HER should be correlated with the ability to perform outer-sphere Co(II/I) ET, since both involve electroactive molecules residing outside the EDL. Our kinetic analysis led to the conclusion that the molecules displaying the outer-sphere Co(II/I) voltammetric wave are minimally HER-active due to a lack of correlation between the Co(II/I) wave integration and HER rates (see above). Since those outside-EDL sites do not appear to be involved in HER, our kinetic analysis implies that the HER process itself does not proceed via an outer-sphere mechanism. The more likely mechanism follows an inner-sphere, or interfacial, CPET pathway in which proton transit across the EDL to bind to the Co site is accompanied by electron transfer from the electrode band states to Co-centered orbitals. Previous experimental and computational studies on Co porphyrins non-specifically adsorbed to carbons point to this type of inner-sphere pathway, which arises because the adsorbed porphyrin resides within the EDL.[25,26] Under this condition, the Co center does not experience any outer-sphere ET processes such as the Co(II/I) because it is at the same electrostatic potential as the carbon surface, and the Co oxidation state remains unchanged until a proton binds directly to the Co and induces electron localization from the carbon to the Co–H bond. Given the stronger surface affinity of phthalocyanines relative to porphyrins,[64–66] we invoke an analogous inner-sphere CPET pathway for CoPc/C and CoFPc/C. This means that the majority of Co sites in our MME films reside within the EDL and are correspondingly OSET-silent and HER-active. In contrast, a minority of sites appear to reside outside the EDL, which are Co(II/I) OSET-active but contribute minimal HER activity. An active site within the EDL also explains how, despite the likely low native hydricity of the putative Co–H intermediate, under polarization the Co–H may still be capable of H_2 formation. Recent studies have shown that polarization can dramatically alter the hydricity of surface-bound species by electrostatically repelling the negatively charged hydride away from the interface to combine with the solution-phase hydride acceptor (e.g., a proton from H_2O).[25,26,67] Overall, our kinetic and mechanistic analyses indicate an inner-sphere nature to the rate-determining CPET step and thereby suggest that HER-active CoPc and CoFPc sites reside within the EDL when adsorbed to carbon.

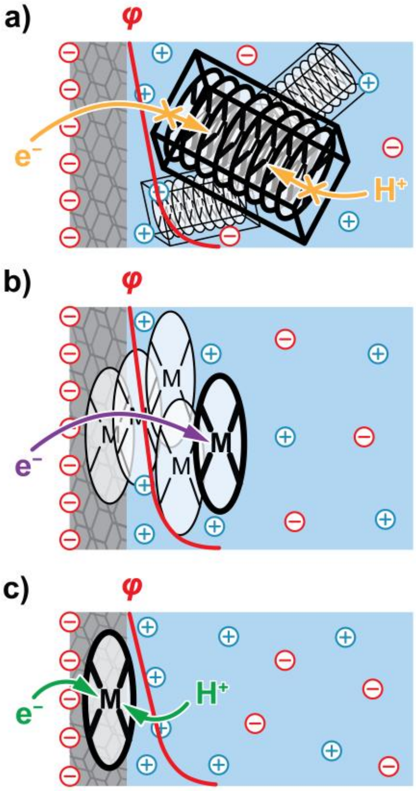

Figure 6. Cartoon representation of each of three molecular subpopulations drawn from the data, with the relevant molecule(s) bolded. **a)** Electrochemically inaccessible sites that are neither able to undergo electron nor proton transfer. **b)** Outer-sphere electron transfer (OSET)-active sites that reside outside the electrochemical double layer (EDL). **c)** OSET-silent sites that reside within the EDL and catalyze HER through a concerted proton-electron transfer (CPET) pathway. The red line represents the electrostatic potential, φ, profile at each interface. This cartoon primarily intends to illustrate the influence of electrostatic polarization on each subpopulation as inferred from the data; there are other possible molecular orientations.

Taken together, the data support the presence of three broad molecular subpopulations, which have been distinguished by varying molecular loadings in the films (**Figure 6**). 1) At high loadings (35 to 75 nmol cm^{-2}), the drop-off in apparent TOF values and transition from 1^{st} to 0^{th} order dependence on Co loading, in conjunction with the micron-scale crystals observed in SEM-EDS images, indicate a population of molecular sites that are electrochemically inaccessible (**Figure 6a**). These sites should be both OSET-silent and HER-inactive, and they may arise from molecules trapped in nonconductive crystals or hydrophobic pockets of the film. While evidence of these inaccessible sites exists at high loadings, they may also be present in low loading films. The loading-dependent HER kinetic analyses, while they furnish invariant TOF values for low loading films, cannot detect any loading-independent constant fraction of inactive sites. Thus, the TOF values based on ICP-MS are lower-limit TOF values. 2) The population of molecular sites that give rise to the Co(II/I) redox feature, the OSET-active sites, comprises 5% to 25% of the total Co loading in the films (**Figure 6b**). Since the loading-dependent HER activity does not scale fully with the OSET-active population, these sites do not contribute detectably to HER activity within the investigated E range. Thus, the data indicate the presence of a minority population of OSET-active molecular sites with minimal HER activity. 3) The remaining OSET-silent sites are assigned as an HER-active population residing within the EDL (**Figure 6c**). The HER activity of the films scales appropriately with the loading of this population, suggesting it is the majority contributor to HER. The mechanistic information laid out in this section thus reports on the HER catalyzed by this population, indicating an inner-sphere, rate-determining Volmer CPET step. While these findings rely on Vulcan XC-72R carbon black for heterogenization, the same effects of adsorption should hold on other carbon black supports. There may be variation in the fractionation of the different molecular subpopulations on different carbons due to variations of surface chemistry (e.g. surface oxidic functionality), yet the electrochemical behavior of each subpopulation should remain the same. Ultimately, studying both the Co(II/I) redox voltammetry and HER activity across a range of molecular loadings allows rough disentanglement of three molecular subpopulations, leading to quantification of reliable lower-limit TOF values and diagnosis of the active site mechanism.

Computation Reveals Compensatory Thermodynamics Along the PCET Pathway

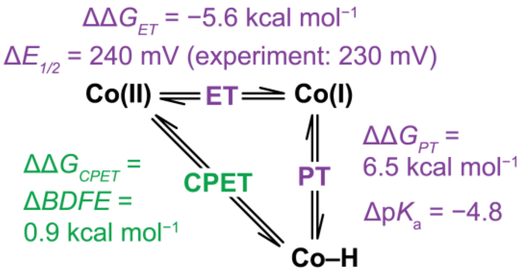

Figure 7. Thermodynamic scheme for the formation of Co–H from Co(II) with computationally-derived parameters. The diagonal leg represents the concerted pathway, while the top and right legs represent the stepwise ET-PT pathway going through the Co(I) intermediate. The thermodynamic values were computed as the ΔG of each step for CoPc and CoFPc individually, and the ΔΔ reported here represents ΔG_{CoFPc} –

ΔG_{CoPc}.

In order to rationalize the finding of inner-sphere CPET-limited HER activity that is roughly independent of $E_{1/2}$, we constructed a thermodynamic scheme for the overall PCET process for forming a Co–H species, the putative HER intermediate formed from a Co(II) initial state (**Figure 7**). Co(II) is taken as the initial state because the oxidation state of an HER-active Co site within the EDL is not reliant on the applied potential of catalysis but instead changes with proton binding.[25,26] The values are presented for each thermodynamic parameter as a difference between the process for CoFPc and the process for CoPc. We have experimentally measured the Co(II/I) $\Delta E_{1/2}$ between the MME systems using the OSET-active subpopulation of sites on the surface. However, the difference in acidity of Co–H (ΔpK_a) and the difference in bond dissociation free energy (ΔBDFE) cannot be readily extracted experimentally, so we turned to computational modeling to obtain estimates of these parameters (see SI for computational details). The carbon surface is excluded from the comparative computational analysis, as we presume surface effects to be roughly similar for CoPc and CoFPc. As a validation of the methodology, the computation recovers a $\Delta\Delta G_{ET}$ of 5.6 kcal mol^{-1}, or 240 meV more favorable ET for Co(II)FPc than Co(II)Pc, which only differs by 10 mV from the experimentally obtained $\Delta E_{1/2}$ for the carbon-adsorbed molecules. Importantly, the computation also reveals that PT to Co(I)Pc is 6.5 kcal mol^{-1} more favorable than PT to Co(I)FPc. The similar and opposite ΔpK_a of the resulting Co–H compensates the large $\Delta E_{1/2}$, thus translating to an overall ΔBDFE of only 0.9 kcal mol^{-1} (40 meV) between CoPc and CoFPc. Strikingly, these computational data indicate that the incorporation of 16 fluoro-substituents serves to move the $E_{1/2}$ and pK_a in compensating directions such that the binding free energy of H to the Co site remains virtually unchanged. These qualitative results are consistent among all levels of theory tested computationally (**Tables S2-4**). Since the Co–H BDFE defines the overall free energy change for CPET, this computational finding rationalizes the similarity in HER activity between CoPc/C and CoFPc/C despite their substantial difference in redox potentials.

Compensation Affects Stepwise and Concerted Pathways Differently

As highlighted in the Introduction, compensation between $\Delta E_{1/2}$ and ΔpK_a that causes a relatively small ΔBDFE for a PCET reaction is well documented across many homogeneous molecular systems.[28–33] However, rates of PCET electrocatalysis still commonly scale with $E_{1/2}$ for homogeneous molecular electrocatalysts,[14–19] whereas we observed a large difference in $E_{1/2}$

without substantial changes in HER activity between CoPc/C and CoFPc/C MMEs. The divergent $E_{1/2}$ dependencies for homogeneous molecular versus MME systems can be understood based on their distinct mechanisms of operation. For the homogeneous molecular case (**Figure 8a**), we will consider a hypothetical PCET pathway proceeding through a quasi-equilibrated ET followed by a rate-determining chemical step PT to the reduced catalyst $\mathbf{M}^{-}$. This hypothetical mechanism would constitute an EC' sequence, as is often invoked for molecular electrocatalysts, in which the C step is a PT to the catalyst.[68–71] For this sequence, even if the BDFE of the M–H intermediate remains unchanged between two catalysts, changes in the $E_{1/2}$ can still manifest in changes in the observed rate. This is because the thermokinetic scale factor, termed the Brønsted α_{PT}, that relates the change in driving force for PT, ΔpK_a, to the change in the barrier height for PT, is often found to be an intermediate value substantially less than 1.[19,72–74] Thus, in the limit of perfect compensation for which $\Delta E_{1/2}$ correlates 1-to-1 with ΔpK_a, a positive shift in $E_{1/2}$ lowers the energy of the reduced intermediate by $-F(\Delta E_{1/2})$ but only increases the barrier height for PT by $F(\alpha_{PT})(\Delta E_{1/2})$. This leads to a reduction in the overall PCET barrier by $-F(1-\alpha_{PT})(\Delta E_{1/2})$ (F is Faraday's constant, see SI Supplemental Note on Stepwise PCET for derivations, **Figure S2**). Consequently, changes to $E_{1/2}$ will lead to changes in the apparent rate constant of catalysis, k_{app}, and correspondingly distinct onset potentials for catalysis (**Figure S2**). Essentially, a more positive $E_{1/2}$ value results in an earlier catalytic onset but a lower maximum k_{app} under this stepwise PCET pathway.

The free energy diagram is substantially different for a hypothetical PCET pathway proceeding through a rate-determining CPET step (**Figure 8b**). Because there is no distinct ET or PT, compensation effects that cause the BDFE to remain unchanged will lead to a common driving force for CPET and correspondingly similar barrier heights as well. This general Bell (Brønsted)-Evans-Polanyi (BEP) principle holds regardless of the inner-sphere or outer-sphere character to the CPET, as long as the CPET is synchronous.[30,75–78] Thus, changes in $E_{1/2}$ are only expected to alter catalytic rates if they also manifest in changes in M–H BDFE, which will translate to changes in barrier height via the BEP scaling factor α_{CPET}. An example of this is the correlation between M(III/II) $E_{1/2}$ and O_2 electroreduction activity by carbon-adsorbed metal macrocycles, where the computed binding energy of O_2 and other intermediates also tracks with $E_{1/2}$.[39] As this discussion highlights, the transition from a stepwise to a concerted PCET pathway leads to a diminished sensitivity to catalyst $E_{1/2}$ and points to alternative principles for catalyst design.

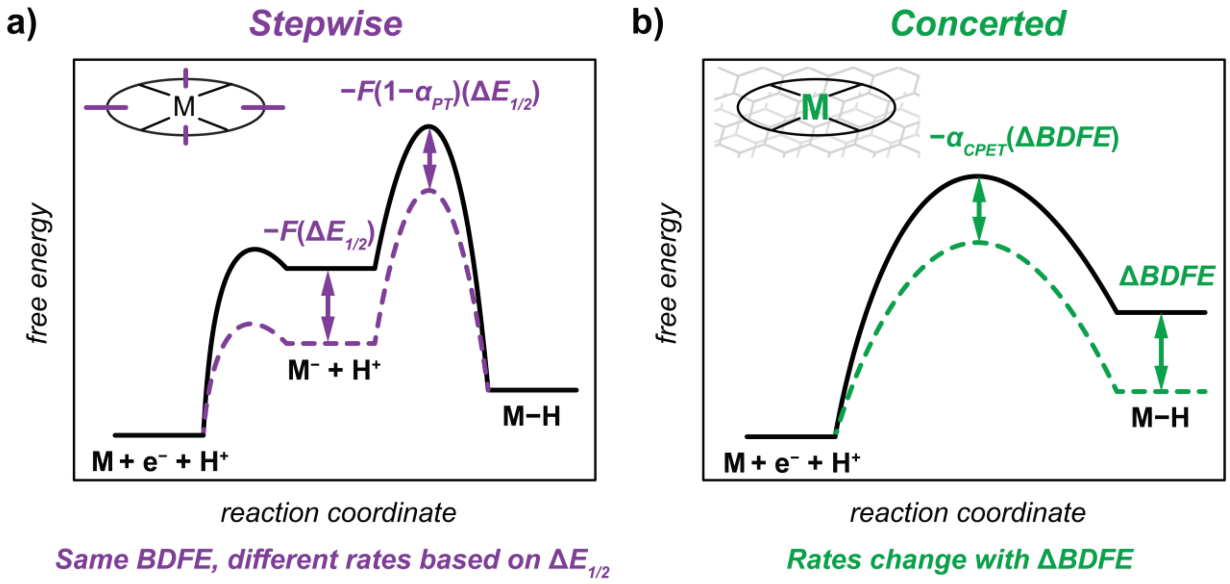

Figure 8. Hypothetical free energy diagrams for a PCET step to form an M–H intermediate. **a)** Stepwise quasi-equilibrated ET followed by rate-determining PT. Purple dotted lines trace an altered free energy landscape for a molecule with a positively shifted $E_{1/2}$ and denote the corresponding changes in the intermediate state energy by $-F(\Delta E_{1/2})$ and in the overall reaction barrier by $-F(1-\alpha_{PT})(\Delta E_{1/2})$, where $0 \leq \alpha_{PT} \leq 1$. The top left cartoon illustrates a homogeneous molecule with purple lines representing electron-withdrawing substituents. **b)** Concerted PCET (CPET). Green dotted lines trace an altered free energy landscape for a molecule with a greater M–H BDFE and the corresponding change in CPET barrier by $-\alpha_{CPET}(\Delta\text{BDFE})$, where $0 \leq \alpha_{CPET} \leq 1$. The top left cartoon illustrates an adsorbed molecule with a green center representing a BDFE-changing substitution.

The foregoing distinction in scaling behavior rationalizes the observed trends for the adsorbed phthalocyanines studied herein. Incorporating 16 fluoro-substituents raises the Co(II/I) $E_{1/2}$ by 230 mV but has a negligible net effect on the Co–H BDFE. Since the Co–H BDFE sets the driving force and barrier height for the rate-determining inner-sphere CPET step, the similarity in this parameter leads to similar catalytic activity across the two MME systems. Thus, the switch from a redox-mediated ET-PT mechanism for a soluble molecule to a non-mediated CPET mechanism for the MME serves to mute the effect of $E_{1/2}$ on catalytic activity.

Conclusions

In order to elucidate design principles for MME electrocatalysts, we present a study on the relevance of molecular $E_{1/2}$ to adsorbed phthalocyanine electrocatalysis. Using HER as a test reaction, we develop a kinetically validated method to estimate active site counts for CoPc/C and

CoFPc/C. Through this analysis, we find two populations of surface molecules: a majority of Co(II/I) OSET-silent molecular sites that correlate with HER activity, and a minority of Co(II/I) OSET-active sites that do not correlate with HER activity. The resulting lower-limit site-normalized HER rates based on total Co loading are similar, despite a 230 mV difference in Co(II/I) $E_{1/2}$ values engendered by the 16 fluoro-substituents. Mechanistic data indicate a rate-determining inner-sphere CPET step, the driving force for which is set by the Co–H BDFE rather than the Co(II/I) $E_{1/2}$. Computational studies indicate that compensatory changes in ΔpK_a and $\Delta E_{1/2}$ lead to Co–H BDFE values that are largely unchanged between CoPc and CoFPc, thereby rationalizing the suppressed effect of substituents on MME electrocatalysis. Considering that many MMEs consist of metal macrocycles strongly adsorbed to carbon surfaces, this finding may hold in any CPET-limited reactivity by those systems.

Despite limited disciplinary intuition over how to tune M–H BDFE, we speculate based on our results that peripheral substitution with electron-donating or -withdrawing groups is insufficient to substantially alter M–H BDFE. Instead, peripheral substituents that alter $E_{1/2}$ but preserve M–H BDFE could serve as an orthogonal handle for changing secondary parameters such as catalyst stability or surface affinity without affecting overall electrocatalytic activity. In contrast, we posit that the primary ligation environment and/or metal identity may be more effective design handles for tuning M–H BDFE and catalytic activity. These results motivate further development of an MME science more similar to traditional surface catalysis, based around the design and understanding of optimal active site–substrate BDFE regimes.

Supporting Information:

Materials; experimental and computational methods; data analysis procedures; catalyst loading data summary; all supporting figures showing complete datasets.

Acknowledgements:

This research was primarily supported by the Department of Energy under award DE-SC0020973. The computational part of this work was supported as part of the Center for Hybrid Approaches in Solar Energy to Liquid Fuels (CHASE), an Energy Innovation Hub funded by the U.S. Department of Energy, Office of Science, Office of Basic Energy Sciences under award number DE-SC0021173. V.M. recognizes support from a National Science Foundation Graduate Research Fellowship under grant DGE-2141064, L.E.S. recognizes support from a National Science

Foundation Graduate Research Fellowship under grant DGE-2444107. V.M. thanks Dr. Bogdan I. Fedeles for ICP-MS support at the Massachusetts Institute of Technology Center for Environmental Health Sciences under a core center grant P30-ES002109 from the National Institute of Environmental Health Sciences, National Institutes of Health. V.M. thanks James M. Daley for SEM-EDS support at MIT.nano facilities. The authors thank the entire Surendranath Lab for their scientific discussions, particularly Dr. Emily A. Boyd and Dr. Jon A. Kephart for manuscript review.

Notes:

The authors declare no competing financial interest.

References:

(1) Murray, R. W. Chemically Modified Electrodes. *Acc. Chem. Res.* **1980**, *13* (5), 135–141. https://doi.org/10.1021/ar50149a002.
(2) Wrighton, M. S. Surface Functionalization of Electrodes with Molecular Reagents. *Science* **1986**, *231* (4733), 32–37. https://doi.org/10.1126/science.231.4733.32.
(3) Abruña, H. D. Coordination Chemistry in Two Dimensions: Chemically Modified Electrodes. *Coord. Chem. Rev.* **1988**, *86*, 135–189. https://doi.org/10.1016/0010-8545(88)85013-6.
(4) Zagal, J. H.; Griveau, S.; Silva, J. F.; Nyokong, T.; Bedioui, F. Metallophthalocyanine-Based Molecular Materials as Catalysts for Electrochemical Reactions. *Coord. Chem. Rev.* **2010**, *254* (23), 2755–2791. https://doi.org/10.1016/j.ccr.2010.05.001.
(5) Bullock, R. M.; Das, A. K.; Appel, A. M. Surface Immobilization of Molecular Electrocatalysts for Energy Conversion. *Chem. – Eur. J.* **2017**, *23* (32), 7626–7641. https://doi.org/10.1002/chem.201605066.
(6) Torbensen, K.; Joulié, D.; Ren, S.; Wang, M.; Salvatore, D.; Berlinguette, C. P.; Robert, M. Molecular Catalysts Boost the Rate of Electrolytic CO2 Reduction. *ACS Energy Lett.* **2020**, *5* (5), 1512–1518. https://doi.org/10.1021/acsenergylett.0c00536.
(7) Shen, Y.; Mu, Y.; Wang, D.; Liu, C.; Diaconescu, P. L. Tuning Electrode Reactivity through Organometallic Complexes. *ACS Appl. Mater. Interfaces* **2023**, acsami.3c01726. https://doi.org/10.1021/acsami.3c01726.
(8) Li, Z.; Zhou, Z.; Sun, M.; Wu, T.; Lu, Q.; Lu, L.; Chen, B.; Chan, C. H.; Wong, H. H.; Huang, B. A Mechanism Review of Metal Phthalocyanines as Single-Atomic Catalysts in Electrochemical Energy Conversion. *Chem. Sci.* **2025**. https://doi.org/10.1039/D5SC03210E.
(9) Boutin, E.; Wang, M.; Lin, J. C.; Mesnage, M.; Mendoza, D.; Lassalle-Kaiser, B.; Hahn, C.; Jaramillo, T. F.; Robert, M. Aqueous Electrochemical Reduction of Carbon Dioxide and Carbon Monoxide into Methanol with Cobalt Phthalocyanine. *Angew. Chem. Int. Ed.* **2019**, *58* (45), 16172–16176. https://doi.org/10.1002/anie.201909257.
(10) Wu, Y.; Jiang, Z.; Lu, X.; Liang, Y.; Wang, H. Domino Electroreduction of CO2 to Methanol on a Molecular Catalyst. *Nature* **2019**, *575* (7784), 639–642. https://doi.org/10.1038/s41586-019-1760-8.

(11) Yu, S.; Yamauchi, H.; Wang, S.; Aggarwal, A.; Kim, J.; Gordiz, K.; Huang, B.; Xu, H.; Zheng, D. J.; Wang, X.; Iriawan, H.; Menga, D.; Shao-Horn, Y. CO2-to-Methanol Electroconversion on a Molecular Cobalt Catalyst Facilitated by Acidic Cations. *Nat. Catal.* **2024**, *7* (9), 1000–1009. https://doi.org/10.1038/s41929-024-01197-2.

(12) Hutchison, P.; Smith, L. E.; Rooney, C. L.; Wang, H.; Hammes-Schiffer, S. Proton-Coupled Electron Transfer Mechanisms for CO2 Reduction to Methanol Catalyzed by Surface-Immobilized Cobalt Phthalocyanine. *J. Am. Chem. Soc.* **2024**, *146* (29), 20230–20240. https://doi.org/10.1021/jacs.4c05444.

(13) Savéant, J.; Costentin, C. *Elements of Molecular and Biomolecular Electrochemistry: An Electrochemical Approach to Electron Transfer Chemistry*, 1st ed.; Wiley, 2019. https://doi.org/10.1002/9781119292364.

(14) Hu, X.; Brunschwig, B. S.; Peters, J. C. Electrocatalytic Hydrogen Evolution at Low Overpotentials by Cobalt Macrocyclic Glyoxime and Tetraimine Complexes. *J. Am. Chem. Soc.* **2007**, *129* (29), 8988–8998. https://doi.org/10.1021/ja067876b.

(15) Kilgore, U. J.; Roberts, J. A. S.; Pool, D. H.; Appel, A. M.; Stewart, M. P.; DuBois, M. R.; Dougherty, W. G.; Kassel, W. S.; Bullock, R. M.; DuBois, D. L. [Ni(PPh2NC6H4X2)2]2+ Complexes as Electrocatalysts for H2 Production: Effect of Substituents, Acids, and Water on Catalytic Rates. *J. Am. Chem. Soc.* **2011**, *133* (15), 5861–5872. https://doi.org/10.1021/ja109755f.

(16) Artero, V.; Savéant, J.-M. Toward the Rational Benchmarking of Homogeneous H2-Evolving Catalysts. *Energy Environ. Sci.* **2014**, *7* (11), 3808–3814. https://doi.org/10.1039/C4EE01709A.

(17) Wang, Y.-H.; Pegis, M. L.; Mayer, J. M.; Stahl, S. S. Molecular Cobalt Catalysts for O2 Reduction: Low-Overpotential Production of H2O2 and Comparison with Iron-Based Catalysts. *J. Am. Chem. Soc.* **2017**, *139* (46), 16458–16461. https://doi.org/10.1021/jacs.7b09089.

(18) Pegis, M. L.; McKeown, B. A.; Kumar, N.; Lang, K.; Wasylenko, D. J.; Zhang, X. P.; Raugei, S.; Mayer, J. M. Homogenous Electrocatalytic Oxygen Reduction Rates Correlate with Reaction Overpotential in Acidic Organic Solutions. *ACS Cent. Sci.* **2016**, *2* (11), 850–856. https://doi.org/10.1021/acscentsci.6b00261.

(19) Pegis, M. L.; Wise, C. F.; Koronkiewicz, B.; Mayer, J. M. Identifying and Breaking Scaling Relations in Molecular Catalysis of Electrochemical Reactions. *J. Am. Chem. Soc.* **2017**, *139* (32), 11000–11003. https://doi.org/10.1021/jacs.7b05642.

(20) Kuwana, T.; Bublitz, D. E.; Hoh, G. Chronopotentiometric Studies on the Oxidation of Ferrocene, Ruthenocene, Osmocene and Some of Their Derivatives1. *J. Am. Chem. Soc.* **1960**, *82* (22), 5811–5817. https://doi.org/10.1021/ja01507a011.

(21) Sim, B. A.; Griller, D.; Wayner, D. D. M. Reduction Potentials for Substituted Benzyl Radicals: pKa Values for the Corresponding Toluenes. *J. Am. Chem. Soc.* **1989**, *111* (2), 754–755. https://doi.org/10.1021/ja00184a066.

(22) Lever, A. B. P. Electrochemical Parametrization of Metal Complex Redox Potentials, Using the Ruthenium(III)/Ruthenium(II) Couple to Generate a Ligand Electrochemical Series. *Inorg. Chem.* **1990**, *29* (6), 1271–1285. https://doi.org/10.1021/ic00331a030.

(23) Jackson, M. N.; Kaminsky, C. J.; Oh, S.; Melville, J. F.; Surendranath, Y. Graphite Conjugation Eliminates Redox Intermediates in Molecular Electrocatalysis. *J. Am. Chem. Soc.* **2019**, *141* (36), 14160–14167. https://doi.org/10.1021/jacs.9b04981.

(24) Jackson, M. N.; Surendranath, Y. Molecular Control of Heterogeneous Electrocatalysis through Graphite Conjugation. *Acc. Chem. Res.* **2019**, *52* (12), 3432–3441. https://doi.org/10.1021/acs.accounts.9b00439.

(25) Kaminsky, C. J.; Weng, S.; Wright, J.; Surendranath, Y. Adsorbed Cobalt Porphyrins Act like Metal Surfaces in Electrocatalysis. *Nat. Catal.* **2022**, *5* (5), 430–442. https://doi.org/10.1038/s41929-022-00791-6.

(26) Hutchison, P.; Kaminsky, C. J.; Surendranath, Y.; Hammes-Schiffer, S. Concerted Proton-Coupled Electron Transfer to a Graphite Adsorbed Metalloporphyrin Occurs by Band to Bond Electron Redistribution. *ACS Cent. Sci.* **2023**, *9* (5), 927–936. https://doi.org/10.1021/acscentsci.3c00186.

(27) Hutchison, P.; Soudackov, A. V.; Hammes-Schiffer, S. Nonadiabatic Proton-Coupled Electron Transfer at a Graphitic Surface Immobilized Cobalt Porphyrin. *ACS Catal.* **2024**, *14* (19), 14363–14372. https://doi.org/10.1021/acscatal.4c03962.

(28) Pratt, D. A.; DiLabio, G. A.; Mulder, P.; Ingold, K. U. Bond Strengths of Toluenes, Anilines, and Phenols: To Hammett or Not. *Acc. Chem. Res.* **2004**, *37* (5), 334–340. https://doi.org/10.1021/ar010010k.

(29) Rennie, B. E.; Eleftheriades, R. G.; Morris, R. H. Systematic Trends in the Electrochemical Properties of Transition Metal Hydride Complexes Discovered by Using the Ligand Acidity Constant Equation. *J. Am. Chem. Soc.* **2020**, *142* (41), 17607–17629. https://doi.org/10.1021/jacs.0c08000.

(30) Agarwal, R. G.; Coste, S. C.; Groff, B. D.; Heuer, A. M.; Noh, H.; Parada, G. A.; Wise, C. F.; Nichols, E. M.; Warren, J. J.; Mayer, J. M. Free Energies of Proton-Coupled Electron Transfer Reagents and Their Applications. *Chem. Rev.* **2022**, *122* (1), 1–49. https://doi.org/10.1021/acs.chemrev.1c00521.

(31) Dhar, D.; Yee, G. M.; Spaeth, A. D.; Boyce, D. W.; Zhang, H.; Dereli, B.; Cramer, C. J.; Tolman, W. B. Perturbing the Copper(III)–Hydroxide Unit through Ligand Structural Variation. *J. Am. Chem. Soc.* **2016**, *138* (1), 356–368. https://doi.org/10.1021/jacs.5b10985.

(32) Chalkley, M. J.; Garrido-Barros, P.; Peters, J. C. A Molecular Mediator for Reductive Concerted Proton-Electron Transfers via Electrocatalysis. *Science* **2020**, *369* (6505), 850–854. https://doi.org/10.1126/science.abc1607.

(33) Groff, B. D.; Cattaneo, M.; Coste, S. C.; Pressley, C. A.; Mercado, B. Q.; Mayer, J. M. Independent Tuning of the pKa or the E1/2 in a Family of Ruthenium Pyridine–Imidazole Complexes. *Inorg. Chem.* **2023**, *62* (26), 10031–10038. https://doi.org/10.1021/acs.inorgchem.3c01241.

(34) Shi, C.; Anson, F. C. Catalytic Pathways for the Electroreduction of Oxygen by Iron Tetrakis(4-N-Methylpyridyl)Porphyrin or Iron Tetraphenylporphyrin Adsorbed on Edge Plane Pyrolytic Graphite Electrodes. *Inorg. Chem.* **1990**, *29* (21), 4298–4305. https://doi.org/10.1021/ic00346a027.

(35) Morozan, A.; Campidelli, S.; Filoramo, A.; Jousselme, B.; Palacin, S. Catalytic Activity of Cobalt and Iron Phthalocyanines or Porphyrins Supported on Different Carbon Nanotubes towards Oxygen Reduction Reaction. *Carbon* **2011**, *49* (14), 4839–4847. https://doi.org/10.1016/j.carbon.2011.07.004.

(36) Rigsby, M. L.; Wasylenko, D. J.; Pegis, M. L.; Mayer, J. M. Medium Effects Are as Important as Catalyst Design for Selectivity in Electrocatalytic Oxygen Reduction by Iron–Porphyrin Complexes. *J. Am. Chem. Soc.* **2015**, *137* (13), 4296–4299. https://doi.org/10.1021/jacs.5b00359.

(37) Birdja, Y. Y.; Vos, R. E.; Wezendonk, T. A.; Jiang, L.; Kapteijn, F.; Koper, M. T. M. Effects of Substrate and Polymer Encapsulation on CO $_2$ Electroreduction by Immobilized Indium(III) Protoporphyrin. *ACS Catal.* **2018**, *8* (5), 4420–4428. https://doi.org/10.1021/acscatal.7b03386.

(38) Haake, M.; Aldakov, D.; Pérard, J.; Veronesi, G.; Tapia, A. A.; Reuillard, B.; Artero, V. Impact of the Surface Microenvironment on the Redox Properties of a Co-Based Molecular Cathode for Selective Aqueous Electrochemical CO2-to-CO Reduction. *J. Am. Chem. Soc.* **2024**, *146* (22), 15345–15355. https://doi.org/10.1021/jacs.4c03089.

(39) Zagal, J. H.; Koper, M. T. M. Reactivity Descriptors for the Activity of Molecular MN4 Catalysts for the Oxygen Reduction Reaction. *Angew. Chem. Int. Ed.* **2016**, *55* (47), 14510–14521. https://doi.org/10.1002/anie.201604311.

(40) Marshall-Roth, T.; Liu, L.; Mannava, V.; Harraz, D. M.; Cook, B. J.; Bullock, R. M.; Surendranath, Y. Shallow Rate-Redox Potential Scaling in Aqueous Molecular Oxygen Reduction Electrocatalysis Across a Family of Iron Macrocycles. *ACS Catal.* **2024**, *14* (24), 18590–18602. https://doi.org/10.1021/acscatal.4c06561.

(41) Shen, J.; Kortlever, R.; Kas, R.; Birdja, Y. Y.; Diaz-Morales, O.; Kwon, Y.; Ledezma-Yanez, I.; Schouten, K. J. P.; Mul, G.; Koper, M. T. M. Electrocatalytic Reduction of Carbon Dioxide to Carbon Monoxide and Methane at an Immobilized Cobalt Protoporphyrin. *Nat. Commun.* **2015**, *6* (1), 8177. https://doi.org/10.1038/ncomms9177.

(42) Shen, J.; Kolb, M. J.; Göttle, A. J.; Koper, M. T. M. DFT Study on the Mechanism of the Electrochemical Reduction of CO2 Catalyzed by Cobalt Porphyrins. *J. Phys. Chem. C* **2016**, *120* (29), 15714–15721. https://doi.org/10.1021/acs.jpcc.5b10763.

(43) Ren, X.; Zhao, J.; Li, X.; Shao, J.; Pan, B.; Salamé, A.; Boutin, E.; Groizard, T.; Wang, S.; Ding, J.; Zhang, X.; Huang, W.-Y.; Zeng, W.-J.; Liu, C.; Li, Y.; Hung, S.-F.; Huang, Y.; Robert, M.; Liu, B. In-Situ Spectroscopic Probe of the Intrinsic Structure Feature of Single-Atom Center in Electrochemical CO/CO2 Reduction to Methanol. *Nat. Commun.* **2023**, *14* (1), 3401. https://doi.org/10.1038/s41467-023-39153-6.

(44) Chan, T.; Zoric, M. R.; Shandilya, A.; Loeb, C. K.; Barrett, J. A.; Cordones, A. A.; Kubiak, C. P. Simple Preparation and Characterization of Hybrid Cobalt Phthalocyanine on Multiwalled Carbon Nanotube Electrodes. *ACS Appl. Energy Mater.* **2024**, *7* (6), 2225–2233. https://doi.org/10.1021/acsaem.3c02953.

(45) Cheon, S.; Li, J.; Wang, H. In Situ Generated CO Enables High-Current CO2 Reduction to Methanol in a Molecular Catalyst Layer. *J. Am. Chem. Soc.* **2024**, *146* (23), 16348–16354. https://doi.org/10.1021/jacs.4c05961.

(46) Ren, S.; Lees, E. W.; Hunt, C.; Jewlal, A.; Kim, Y.; Zhang, Z.; Mowbray, B. A. W.; Fink, A. G.; Melo, L.; Grant, E. R.; Berlinguette, C. P. Catalyst Aggregation Matters for Immobilized Molecular CO2RR Electrocatalysts. *J. Am. Chem. Soc.* **2023**, *145* (8), 4414–4420. https://doi.org/10.1021/jacs.2c08380.

(47) Zhu, Q.; Rooney, C. L.; Shema, H.; Zeng, C.; Panetier, J. A.; Gross, E.; Wang, H.; Baker, L. R. The Solvation Environment of Molecularly Dispersed Cobalt Phthalocyanine Determines Methanol Selectivity during Electrocatalytic CO2 Reduction. *Nat. Catal.* **2024**, *7* (9), 987–999. https://doi.org/10.1038/s41929-024-01190-9.

(48) Favero, S.; Li, A.; Wang, M.; Uddin, F.; Kuzuoglu, B.; Georgeson, A.; Stephens, I. E. L.; Titirici, M. M. Poly(Ionic Liquid) Ionomers Help Prevent Active Site Aggregation, in Single-Site Oxygen Reduction Catalysts. *ACS Catal.* **2024**, *14* (10), 7937–7948. https://doi.org/10.1021/acscatal.4c01418.

(49) Dean, W. S.; Soucy, T. L.; Rivera-Cruz, K. E.; Filien, L. L.; Terry, B. D.; McCrory, C. C. L. Mitigating Cobalt Phthalocyanine Aggregation in Electrocatalyst Films through Codeposition with an Axially Coordinating Polymer. *Small* **2025**, *21* (7), 2402293. https://doi.org/10.1002/smll.202402293.

(50) Artero, V.; Chavarot-Kerlidou, M.; Fontecave, M. Splitting Water with Cobalt. *Angew. Chem. Int. Ed.* **2011**, *50* (32), 7238–7266. https://doi.org/10.1002/anie.201007987.

(51) Thoi, V. S.; Sun, Y.; Long, J. R.; Chang, C. J. Complexes of Earth-Abundant Metals for Catalytic Electrochemical Hydrogen Generation under Aqueous Conditions. *Chem. Soc. Rev.* **2013**, *42* (6), 2388–2400. https://doi.org/10.1039/C2CS35272A.

(52) Beyene, B. B.; Mane, S. B.; Hung, C.-H. Highly Efficient Electrocatalytic Hydrogen Evolution from Neutral Aqueous Solution by a Water-Soluble Anionic Cobalt(II) Porphyrin. *Chem. Commun.* **2015**, *51* (81), 15067–15070. https://doi.org/10.1039/C5CC05582B.

(53) Beyene, B. B.; Mane, S. B.; Hung, C.-H. Electrochemical Hydrogen Evolution by Cobalt (II) Porphyrins: Effects of Ligand Modification on Catalytic Activity, Efficiency and Overpotential. *J. Electrochem. Soc.* **2018**, *165* (9), H481. https://doi.org/10.1149/2.0481809jes.

(54) Xu, G.; Lei, H.; Zhou, G.; Zhang, C.; Xie, L.; Zhang, W.; Cao, R. Boosting Hydrogen Evolution by Using Covalent Frameworks of Fluorinated Cobalt Porphyrins Supported on Carbon Nanotubes. *Chem. Commun.* **2019**, *55* (84), 12647–12650. https://doi.org/10.1039/C9CC06916J.

(55) Rooney, C. L.; Lyons, M.; Wu, Y.; Hu, G.; Wang, M.; Choi, C.; Gao, Y.; Chang, C.-W.; Brudvig, G. W.; Feng, Z.; Wang, H. Active Sites of Cobalt Phthalocyanine in Electrocatalytic CO2 Reduction to Methanol. *Angew. Chem. Int. Ed.* **2024**, *63* (2), e202310623. https://doi.org/10.1002/anie.202310623.

(56) Yao, L.; Rivera-Cruz, K. E.; Zimmerman, P. M.; Singh, N.; McCrory, C. C. L. Electrochemical CO2 Reduction to Methanol by Cobalt Phthalocyanine: Quantifying CO2 and CO Binding Strengths and Their Influence on Methanol Production. *ACS Catal.* **2024**, *14* (1), 366–372. https://doi.org/10.1021/acscatal.3c04957.

(57) Zecevic, S.; Simic-Glavaski, B.; Yeager, E.; Lever, A. B. P.; Minor, P. C. Spectroscopic and Electrochemical Studies of Transition Metal Tetrasulfonated Phthalocyanines: Part V. Voltammetric Studies of Adsorbed Tetrasulfonated Phthalocyanines (MTsPc) in Aqueous Solutions. *J. Electroanal. Chem. Interfacial Electrochem.* **1985**, *196* (2), 339–358. https://doi.org/10.1016/0022-0728(85)80032-2.

(58) Ouyang, J.; Shigehara, K.; Yamada, A.; Anson, F. C. Hexadecafluoro- and Octacyano Phthalocyanines as Electrocatalysts for the Reduction of Dioxygen. *J. Electroanal. Chem. Interfacial Electrochem.* **1991**, *297* (2), 489–498. https://doi.org/10.1016/0022-0728(91)80043-P.

(59) Yoshida, T.; Kamato, K.; Tsukamoto, M.; Iida, T.; Schlettwein, D.; Wöhrle, D.; Kaneko, M. Selective Electroacatalysis for CO2 Reduction in the Aqueous Phase Using Cobalt Phthalocyanine/Poly-4-Vinylpyridine Modified Electrodes. *J. Electroanal. Chem.* **1995**, *385* (2), 209–225. https://doi.org/10.1016/0022-0728(94)03762-R.

(60) Madon, R. J.; Boudart, M. Experimental Criterion for the Absence of Artifacts in the Measurement of Rates of Heterogeneous Catalytic Reactions. *Ind. Eng. Chem. Fundam.* **1982**, *21* (4), 438–447. https://doi.org/10.1021/i100008a022.

(61) Goldsmith, Z. K.; Lam, Y. C.; Soudackov, A. V.; Hammes-Schiffer, S. Proton Discharge on a Gold Electrode from Triethylammonium in Acetonitrile: Theoretical Modeling of Potential-Dependent Kinetic Isotope Effects. *J. Am. Chem. Soc.* **2019**, *141* (2), 1084–1090. https://doi.org/10.1021/jacs.8b11826.

(62) Jackson, M. N.; Surendranath, Y. Donor-Dependent Kinetics of Interfacial Proton-Coupled Electron Transfer. *J. Am. Chem. Soc.* **2016**, *138* (9), 3228–3234. https://doi.org/10.1021/jacs.6b00167.

(63) Hammes-Schiffer, S. Explaining Kinetic Isotope Effects in Proton-Coupled Electron Transfer Reactions. *Acc. Chem. Res.* **2025**, *58* (8), 1335–1344. https://doi.org/10.1021/acs.accounts.5c00119.

(64) Gottfried, J. M. Surface Chemistry of Porphyrins and Phthalocyanines. *Surf. Sci. Rep.* **2015**, *70* (3), 259–379. https://doi.org/10.1016/j.surfrep.2015.04.001.

(65) Hipps, K. W.; Mazur, U. Kinetic and Thermodynamic Control in Porphyrin and Phthalocyanine Self-Assembled Monolayers. *Langmuir* **2018**, *34* (1), 3–17. https://doi.org/10.1021/acs.langmuir.7b02672.

(66) Feng, S.; Luo, N.; Tang, A.; Chen, W.; Zhang, Y.; Huang, S.; Dou, W. Phthalocyanine and Metal Phthalocyanines Adsorbed on Graphene: A Density Functional Study. *J. Phys. Chem. C* **2019**, *123* (27), 16614–16620. https://doi.org/10.1021/acs.jpcc.8b11757.

(67) Wang, H.-X.; Toh, W. L.; Tang, B. Y.; Surendranath, Y. Metal Surfaces Catalyse Polarization-Dependent Hydride Transfer from H2. *Nat. Catal.* **2023**, *6* (4), 351–362. https://doi.org/10.1038/s41929-023-00944-1.

(68) Huynh, M. H. V.; Meyer, T. J. Proton-Coupled Electron Transfer. *Chem. Rev.* **2007**, *107* (11), 5004–5064. https://doi.org/10.1021/cr0500030.

(69) Helm, M. L.; Stewart, M. P.; Bullock, R. M.; DuBois, M. R.; DuBois, D. L. A Synthetic Nickel Electrocatalyst with a Turnover Frequency Above 100,000 S−1 for H2 Production. *Science* **2011**, *333* (6044), 863–866. https://doi.org/10.1126/science.1205864.

(70) Costentin, C.; Drouet, S.; Robert, M.; Savéant, J.-M. Turnover Numbers, Turnover Frequencies, and Overpotential in Molecular Catalysis of Electrochemical Reactions. Cyclic Voltammetry and Preparative-Scale Electrolysis. *J. Am. Chem. Soc.* **2012**, *134* (27), 11235–11242. https://doi.org/10.1021/ja303560c.

(71) Elgrishi, N.; McCarthy, B. D.; Rountree, E. S.; Dempsey, J. L. Reaction Pathways of Hydrogen-Evolving Electrocatalysts: Electrochemical and Spectroscopic Studies of Proton-Coupled Electron Transfer Processes. *ACS Catal.* **2016**, *6* (6), 3644–3659. https://doi.org/10.1021/acscatal.6b00778.

(72) Kresge, A. J. The Brønsted Relation – Recent Developments. *Chem. Soc. Rev.* **1973**, *2* (4), 475–503. https://doi.org/10.1039/CS9730200475.

(73) Wang, Y.-H.; Schneider, P. E.; Goldsmith, Z. K.; Mondal, B.; Hammes-Schiffer, S.; Stahl, S. S. Brønsted Acid Scaling Relationships Enable Control Over Product Selectivity from O2 Reduction with a Mononuclear Cobalt Porphyrin Catalyst. *ACS Cent. Sci.* **2019**, *5* (6), 1024–1034. https://doi.org/10.1021/acscentsci.9b00194.

(74) Montgomery, C. L.; Amtawong, J.; Jordan, A. M.; Kurtz, D. A.; Dempsey, J. L. Proton Transfer Kinetics of Transition Metal Hydride Complexes and Implications for Fuel-Forming Reactions. *Chem. Soc. Rev.* **2023**, *52* (20), 7137–7169. https://doi.org/10.1039/D3CS00355H.

(75) Bronsted, J. N. Acid and Basic Catalysis. *Chem. Rev.* **1928**, *5* (3), 231–338. https://doi.org/10.1021/cr60019a001.

(76) Evans, M. G.; Polanyi, M. Some Applications of the Transition State Method to the Calculation of Reaction Velocities, Especially in Solution. *Trans. Faraday Soc.* **1935**, *31* (0), 875–894. https://doi.org/10.1039/TF9353100875.
(77) Evans, M. G.; Polanyi, M. Inertia and Driving Force of Chemical Reactions. *Trans. Faraday Soc.* **1938**, *34* (0), 11–24. https://doi.org/10.1039/TF9383400011.
(78) Mayer, J. M. Bonds over Electrons: Proton Coupled Electron Transfer at Solid–Solution Interfaces. *J. Am. Chem. Soc.* **2023**, *145* (13), 7050–7064. https://doi.org/10.1021/jacs.2c10212.

Supporting Information

Concerted Proton-Electron Transfer Minimizes Substituent Effects on Adsorbed Phthalocyanine Electrocatalysis

Vennela Mannava[1], Logan E. Smith[2], Joel G. Gardner[1], Sharon Hammes-Schiffer[2], and Yogesh Surendranath[1]*

[1]Department of Chemistry, Massachusetts Institute of Technology, Cambridge, Massachusetts 02139, United States
[2]Department of Chemistry, Princeton University, Princeton, New Jersey 08544, United States

*Corresponding author: yogi@mit.edu

Table of Contents

Experimental Methods

Chemicals and materials. Dimethylformamide (anhydrous, 99.8%) and ethanol (200 proof, 99.5%) were obtained from Millipore Sigma. Heptanes (99.0%) was obtained from Macron Fine Chemicals. All electrochemistry used Milli-Q H_2O (Millipore Type 1, 18.2 MΩ-cm resistivity) or, where noted, D_2O (Cambridge Isotope Laboratories, Inc, 99.9%). Electrolytes were prepared from the following: sodium hydroxide (BeanTown Chemical, 99.99 % trace metals basis), perchloric acid (Millipore Sigma, 70% in water, 99.999% trace metals basis), boric acid (Alfa Aesar, 99.9995% trace metals basis), sodium phosphate dibasic (Millipore Sigma, anhydrous, 99.999% trace metals basis), sodium acetate (Alfa Aesar, anhydrous, 99.997%), and sodium perchlorate hydrate (Millipore Sigma, 99.99%). Cobalt(II) phthalocyanine (CoPc, β-form, 97%) was obtained from Millipore Sigma. Cobalt(II) 1,2,3,4,8,9,10,11,15,16,17,18,22,23,24,25-hexadecafluoro-29H,31H-phthalocyanine (CoFPc, 98%) was obtained from Ambeed. Cobalt(II) chloride hexahydrate ($CoCl_2$, 98%) was obtained from VWR. Zinc phthalocyanine (ZnPc, 97%) was obtained from Millipore Sigma. 5 wt.% perfluorinated Nafion^{TM} resin solution (LIQUION LQ-1105 1100EW 5 wt.%, in 20 wt % water and 75 wt % *n*-PrOH/*i*-PrOH) was obtained from Ion Power Inc. Vulcan XC-72R carbon black powder (C) was obtained from Cabot Corporation. All chemicals and materials listed above were used as received.

General electrochemical methods. All electrochemical experiments were performed at ambient conditions using a Biologic VSP 16-channel potentiostat. Rotation experiments were performed using a Metrohm Autolab RDE-2. A Hg/HgO reference electrode was used as received from CH Instruments, Inc and was stored in 1 M NaOH (BeanTown Chemical, 99.99 % trace metals basis) prior to use. The reference electrode was periodically checked against a pristine Ag/AgCl reference to correct for any drift. Electrode potentials for experiments conducted in aqueous media were plotted vs the standard hydrogen electrode (SHE) using the following conversion equation: $E_{SHE} = E_{Hg/HgO} + 0.140$. Cell resistance was measured using the Biologic Current Interrupt method and 80% compensation was applied to experiments where *iR* losses were > 5 mV. Glassy carbon disk electrodes (5 mm diameter) were obtained from Pine Research Instrumentation, Inc. A Pt mesh was used as the counter electrode for all experiments and was treated with aqua regia prior to use. An aqua regia-treated Ti mesh can also be used to obtain identical results. All experiments were conducted in a custom 5-neck cell equipped with a sparge tube and counter compartment separated by a glass frit. All glassware used for electrochemical measurements was soaked in aqua regia for at least 30 minutes and thoroughly washed with reagent-grade water prior to use. All experiments were conducted under Ar flow (after a pre-sparge of at least 15 min) with electrode rotation at 2000 R.P.M. All experiments, unless otherwise noted, were conducted in 0.1 M NaOH with a pH 13 ±0.1 as determined by a Thermo Scientific Orion 3-Star pH meter. For experiments in other pH conditions, a Britton-Robinson buffer was prepared containing 0.04 M each of sodium acetate, sodium phosphate and boric acid, as well as 0.05 M sodium perchlorate. The buffer was titrated with 1 M solutions of NaOH and $HClO_4$ to reach the desired pH level.

Preparation of molecularly modified electrode (MME) films.

Glassy carbon disk electrodes were soaked in freshly made aqua regia for 10 seconds, then rinsed with Milli-Q H_2O. Electrodes were polished by hand on MasterTex pads (JH Technologies) using MetaDi Supreme polycrystalline diamond suspensions (JH Technologies) of 1 μm, 0.25 μm, and

0.05 μm size sequentially, interspersed with Milli-Q H_2O and EtOH rinses. The final rinse included 10 min sonication in a 1:1 mixture of Milli-Q H_2O and EtOH.

High catalyst loading inks (>0.3 mg total) were prepared by weighing out the desired mass on a microbalance into a 4-dram vial. 0.7 mL DMF was added to the catalyst vial. 2.5 mg Vulcan XC-72R carbon black powder was dispersed in 0.2 mL DMF in a separate 4-dram vial. Both vials were sonicated for 25 min (**Figure S1**, step 1). Subsequently, the entire catalyst dispersion was pipetted into the carbon dispersion such that the total volume was 0.9 mL DMF (**Figure S1**, step 2). This combined suspension was further sonicated for 25 min. Then 0.1 mL 5 wt% Nafion solution was added, and the entire 1 mL ink was sonicated for 20 min (**Figure S1**, step 3). The ink was allowed to rest for 30-60 min then sonicated again for an additional 20 min. In a well-dispersed ink, the liquid is visibly indistinguishable from the solid. 10 μL of this ink was dropcast onto each polished glassy carbon disk electrode (**Figure S1**, step 4). The resulting catalyst films were dried in an 80 °C oven for 30-60 min.

Low catalyst loading inks (<0.3 mg total) were prepared by dispersing 3 mg (CoPc) or 6 mg (CoFPc) into 30 mL DMF. These suspensions were sonicated for at least 60 min, until the solution was darkly colored and undissolved solid appeared finely dispersed with no visible large aggregates (**Figure S1**, step 1). 2.5 mg Vulcan XC-72R carbon black powder was dispersed in [0.9 – *x*] mL DMF in a 4-dram vial. Both vials were sonicated for 25 min. Then *x* mL ($x = 0.3$ to 0.8 mL) catalyst dispersion, based on the desired amount of total catalyst, was pipetted into the carbon dispersion such that the total volume was 0.9 mL DMF (**Figure S1**, step 2). This was sonicated for 25 min. Then 0.1 mL 5 wt% Nafion solution was added, and the entire 1 mL ink was sonicated for 20 min (**Figure S1**, step 3). The ink was allowed to rest for 30-60 min then sonicated again for 20 min. In a well-dispersed ink, the liquid is visibly indistinguishable from the solid. 10 μL of the ink was dropcast onto each polished glassy carbon disk electrode (**Figure S1**, step 4). The resulting catalyst films were dried in an 80 °C oven for 30-60 min.

Half-thickness films were prepared by dropcasting 5 μL of a low catalyst loading ink (total 0.05 mg CoPc or 0.1 mg CoFPc) instead of 10 μL. $CoCl_2$/C films were prepared by using a solution of 0.7 mg cobalt(II) chloride hexahydrate in 3 mL DMF sonicated for 30 min until fully dissolved. Then 0.13 mL were added to the usual C dispersion (in 0.77 mL DMF this time) and the remaining ink and film preparation followed as described above. ZnPc/C films were prepared by dissolving 0.9 mg ZnPc in 0.7 mL DMF and combining with a 2.5 mg C dispersion in 0.2 mL DMF. The remaining ink and film preparation followed as described above. Unmodified C films were prepared by adding the entire 0.9 mL DMF to 2.5 mg Vulcan XC-72R carbon black powder without any catalyst, and the remaining ink and film preparation followed as described above.

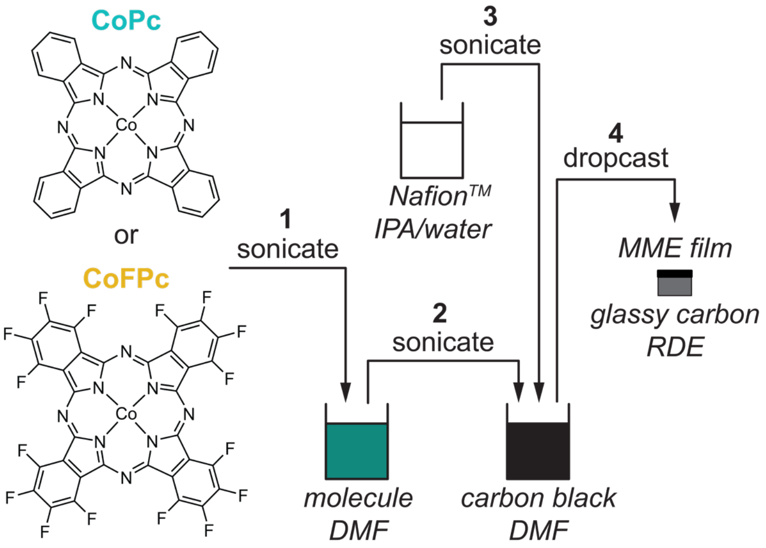

Figure S1. Stepwise procedure for preparing CoPc/C or CoFPc/C MME films. The numbers correspond to the chronological sequence as described in the text.

Determination of catalyst loading.

Methods for inductively coupled plasma – mass spectrometry (ICP-MS).

Spectra were collected using an Agilent 7900 ICP-MS. A calibration curve was generated from aqueous 2% nitric acid solutions containing known concentrations of Co. The calibration solution series was prepared by serial dilution of a Co standard solution (Fluka, TraceCERT 1000 ppm in 2% HNO_3) with 2% nitric acid (VWR Chemicals BDH, 67-70% Aristar Ultra for trace metal analysis). All volumetric flasks were soaked in aqua regia and rinsed with copious amounts of Milli-Q H_2O prior to use. Solutions, if not used immediately, were stored in air-tight HDPE plastic containers and shielded from light.

After the electrochemical experiments, each electrode was left in the PTFE holder and suspended upside down in a 15 mL plastic centrifuge tube containing 1 mL of DMF such that the entire film surface contacted the liquid. This tube was sonicated for 20 min such that all of the C film had delaminated from the electrode and entered the liquid. A tweezer was used to remove the electrode & holder from the tube, with 0.2 mL of DMF rinse of the electrode surface being recollected in the tube. The electrode surface was then wiped with a Kimwipe to check that no carbon black had been left behind to stain the Kimwipe. The 1.2 mL of DMF containing the film components was rinsed into a 20 mL vial with an additional 2-3 mL heptanes. All of the liquid was then removed by blowing a gentle stream of N_2 over the vial while heating in a vial block at 85-90 °C, leaving behind black solid and pale yellowish residues.

Approximately 12 to 16 hours before the ICP-MS run, 1 mL of high-purity concentrated nitric acid was added to each sample vial and capped tightly. Each vial was sonicated for 5 min to dislodge solids. The films were allowed to digest in the acid for 18 to 22 hours. Then the acid was filtered carefully through a 0.22 µm PTFE syringe filter (Foxx EZFlow) to remove large particles. 0.3 mL of the filtrate was then diluted in 10 mL of Milli-Q water in a volumetric flask and transferred into a 15 mL plastic tube for analysis. All samples were analyzed within hours after preparation, since prolonged exposure of the Co sample to polypropylene plastic tubes led to gradual loss of Co signal observed by ICP-MS, ~15% after 3 days.

Methods for cyclic voltammetry (CV) integration.

CV scans were collected in 0.1 M NaOH in H_2O (pH 13) under Ar at 2000 R.P.M. CV scans were initiated at the open circuit potential (OCP) and swept in the negative direction at scan rates of 100 or 300 mV s^{-1} until successive cycles overlaid, which required at least 2-3 cycles. One subsequent cycle was collected at 5 mV s^{-1} (CoPc/C) or 100 mV s^{-1} (CoFPc/C) which was used for integration of the redox peak. The Biologic EC-Lab software CV peak integration tool with linear baseline was used to determine the charge passed. The integrated charge in the Co(II/I) wave (*Q*) was converted to moles of electrons by dividing by Faraday's constant (*F*), then a 1:1 Co to e^- ratio was assumed to obtain the population of Co(II/I) outer-sphere electron transfer (OSET)-active molecules in each MME film, divided by the geometric electrode surface area.

$$OSETactive\,[nmol\ cm^{-2}] = \frac{Q\,[C]}{F\,[C\ mol_{e-}{}^{-1}]} * \frac{1\,[mol_{Co}]}{1\,[mol_{e-}]} * \frac{10^9\,[nmol]}{1\,[mol]} * \frac{1}{0.196\,[cm^2]}$$

Table S1. Catalyst loading data summary.

Catalyst Addition[a]	Nominal Film Catalyst Loading (nmol cm^{-2})[b]	ICP-MS Film Co Loading (nmol cm^{-2})[c]	Co(II/I) CV Response Integration (nmol cm^{-2})[c]
0.3 mL of stock (3 mg CoPc in 30 mL of DMF)	2.7	3.1 – 3.8	0.50 – 0.52
0.5 mL of stock (3 mg CoPc in 30 mL of DMF)	4.5	4.9 – 5.5	0.94 – 1.1
0.8 mL of stock (3 mg CoPc in 30 mL of DMF)	7.1	6.2 – 6.2	1.4 – 1.5
0.4 mg CoPc in 0.7 mL of DMF	36	37 – 38	3.1 – 3.6
0.9 mg CoPc in 0.7 mL of DMF	80	67 – 71	3.1 – 3.4
0.5 mL of stock (6 mg CoFPc in 30 mL of DMF)	5.9	5.8 – 6.5	0.52 – 0.57
0.55 mL of stock (6 mg CoFPc in 30 mL of DMF)	6.5	6.7 – 7.7	0.58 – 0.62
0.7 mL of stock (6 mg CoFPc in 30 mL of DMF)	8.3	8.5 – 9.3	0.65 – 0.70
0.7 mg CoFPc in 0.7 mL of DMF	42	36 – 38	4.3 – 4.8
1.3 mg CoFPc in 0.7 mL of DMF	77	66 – 75	2.3 – 3.1
0 mg (C film)	0	0.08 – 0.09	N/A

[a]All other MME film preparation details are noted in **Preparation of molecularly modified electrode (MME) films.** [b]Nominal loading was calculated by dividing the total catalyst added to the ink by 100 (using 10 µL of a 1 mL ink per film) and by the geometric electrode surface area (0.196 cm^2). [c]Data are listed as a range from lowest to highest measured values for replicate films from one ink. Note that all *TOF* calculations use only the measured ICP-MS values.

Scanning Electron Microscopy - Energy Dispersive X-ray Spectroscopy (SEM-EDS).

SEM and SEM-EDS images were collected using a Zeiss Gemini 450 Scanning Electron Microscope equipped with an Everhart Thornley Secondary Electron Detector and InLens Secondary Electron Detector. Film samples were affixed to SEM stubs using double-sided carbon tape on the bottom of the glassy carbon disk electrode. SEM images were collected using an accelerating voltage of 10 to 15 kV in high vacuum mode. SEM-EDS images were collecting using an accelerating voltage of 15 kV. EDS maps were collected using an Aztec EDS detector add-on to the Zeiss Gemini 450 SEM.

Assessment of hydrogen evolution reaction (HER) activity.

Evaluation of catalysis in basic aqueous media.

Steady-state data were collected via a series of chronoamperometry experiments across a random sequence of applied potentials spanning the activation-controlled region for HER catalysis. Each chronoamperogram was allowed to reach steady state (20-30 seconds), and the average current density (j_{av}) over the last 5 seconds of data collection was divided by Faraday's constant (F) and the ICP-MS measured Co content (Co) assuming a 2 e$^-$ per Co ratio for HER to determine the *TOF* at each potential.

$$TOF\ [s^{-1}] = \frac{|j_{av}\ [mC\ s^{-1}\ cm^{-2}]|}{F\ \left[C\ mol_{e-}{}^{-1}\right]} * \frac{1\ [A]}{10^3\ [mA]} * \frac{1}{Co\ [nmol_{Co}\ cm^{-2}]} * \frac{10^9\ [nmol]}{1\ [mol]} * \frac{1\ [mol_{Co}]}{2\ [mol_{e-}]}$$

The chronoamperograms used for *TOF* analysis were taken only after conducting a linear sweep voltammogram from open circuit potential to −1.23 V vs SHE and a prior chronoamperometry sequence, in order to ensure stable film wetting and rapid current equilibration. After these pre-activation steps, all future chronoamperograms produced consistent steady-state data.

Every piece of data (electrochemical & ICP-MS) was collected on each CoPc/C or CoFPc/C film in order to provide a full independent dataset per film. Linear fits of the data were always conducted on the unaggregated data to get slopes, intercepts, and fit errors. For **Figures 3-4** and **S23-24**, the data were aggregated into triplicates based on common ICP-MS loadings to plot an average and standard deviation, although the linear fits and fit errors shown are always from the original unaggregated data.

H/D Kinetic Isotope Effect (KIE).

0.1 M NaOH electrolytes were prepared by adding 80 mg NaOH (BeanTown Chemical, 99.99 % trace metals basis) to 20.0 mL of H_2O or D_2O (Cambridge Isotope Laboratories, Inc, 99.9%). Although the D_2O electrolyte included NaOH, it was still 99.8% D, so we take the HER current as originating entirely from D_2O. Steady-state data were collected and analyzed to obtain *TOF* values in each electrolyte as described in the prior section. Fresh films were used for each experiment, and the Co loadings per film were kept similar between H_2O and D_2O experiments to ensure the same regime of HER activity (6.2 ± 0.02 nmol cm^{-2} in H_2O and 6.5 ± 0.51 nmol cm^{-2} in D_2O for CoPc/C; 7.2 ± 0.53 nmol cm^{-2} in H_2O and 7.4 ± 0.38 nmol cm^{-2} in D_2O for CoFPc/C). The *TOF* average and standard deviation for triplicate films in each electrolyte were then divided to generate the $TOF_H\ TOF_D^{-1}$ average and standard deviation, using the standard statistical method for dividing two values with associated standard deviations.

Computational methods.

All calculations were performed with the Gaussian16 electronic structure program.[1] The calculations were conducted with the BP86 exchange correlation functional[2,3] with Grimme's D3 corrections.[4] The BP86 functional was chosen as it has previously predicted the correct ground state spins for cobalt porphyrins and accurately predicted redox potentials and pK_a's for similar cobalt electrocatalysts.[5,6] Additionally, the BP86 functional captures the experimentally observed metal-centered reduction of Co(II)Pc to Co(I)Pc.[7] The LANL2DZ basis set[8–10] was used on the Co metal center, and the 6-31G(d,p) basis set was used on all other elements.[11–13] Implicit water solvent was modeled with the conductor-like polarizable continuum model (C-PCM)[14,15] with a dielectric constant of 78.3 and non-electrostatic terms consisting of the solute-solvent repulsion and dispersion interaction energy and solute cavitation energy. The molecular cavity was generated with the Gaussian16 default radii from the Universal Force Field (UFF).[16] This level of theory was found to agree well with experimental observations on the CO_2 reduction chemistry for immobilized CoPc.[17] The geometries were optimized and confirmed to be true minima with analysis showing no vibrational modes with imaginary frequencies. To test the consistency of the observed trends, additional calculations were conducted with the B3LYP-D3,[4,18–21] PBE-D3,[3,4] and M06-L-D3[4,22] functionals. Calculations with alternative basis sets for both main group elements and the cobalt center were also performed for comparison. The impact of solvation model on the relative free energies was evaluated by using Bondi atomic radii[23] for molecular cavity generation with the C-PCM approach and by using the SMD solvation model.[24] Relative free energies for sequential electron transfer (ET) and proton transfer (PT) as well as the concerted proton-electron transfer (CPET) process were calculated as $\Delta G_{CoFPc} - \Delta G_{CoPc}$. The free energies include zero-point energy and entropic contributions.

Impact of functional, basis set, and solvation model on calculated thermodynamics

The trend that Δ*BDFE* between CoFPc and CoPc remains small due to the compensatory ΔpK_a and $\Delta E_{1/2}$ is consistent across all levels of theory tested (**Tables S2-4**), with the CPET free energies, corresponding to Δ*BDFE*, differing only by around 1 kcal/mol.

Table S2. Calculated Relative Free Energy Differences (kcal mol^{-1}) for ET, PT, and CPET with Different Functionals[a]

Functional	ΔΔ*G* ET	ΔΔ*G* PT	ΔΔ*G* CPET
BP86	−5.6[b]	6.5[b]	0.9[b]
B3LYP	−7.2	8.4	1.2
PBE	−5.3	6.1	0.8
M06-L	−6.2	7.0	0.8

[a]$\Delta\Delta G$ calculated as $\Delta G_{CoFPc} - \Delta G_{CoPc}$ using the LANL2DZ basis set for Co, 6-31G(d,p) basis set for C, N, and H, BP86-D3 functional, and C-PCM with UFF radii. [b]Values reported in **Figure 7.**

Table S3. Calculated Relative Free Energy Differences (kcal mol^{-1}) for ET, PT, and CPET with Different Basis Sets[a]

Co Basis Set	C, N, H Basis set	$\Delta\Delta G$ ET	$\Delta\Delta G$ PT	$\Delta\Delta G$ CPET
LANL2DZ	6-31G(d,p)	−5.6	6.5	0.9
SDD[23]	6-31G(d,p)	−5.6	6.4	0.8
LANL2DZ	6-311G(d,p)	−6.5	7.4	0.9
LANL2DZ	6-31+G(d,p)	−7.8	8.9	1.1
LANL2DZ	6-311++G(d,p)	−7.8	8.8	1.0

[a]$\Delta\Delta G$ calculated as $\Delta G_{CoFPc} - \Delta G_{CoPc}$ using the BP86-D3 functional and C-PCM with UFF radii.

Table S4. Calculated Relative Free Energy Differences (kcal mol^{-1}) for ET, PT, and CPET with Different Implicit Water Solvation Models[a]

Solvent Model	$\Delta\Delta G$ ET	$\Delta\Delta G$ PT	$\Delta\Delta G$ CPET
C-PCM (UFF)[b]	−5.6	6.5	0.9
C-PCM (Bondi)[b]	−4.6	5.2	0.6
SMD	−4.8	5.8	1.0

[a]$\Delta\Delta G$ calculated as $\Delta G_{CoFPc} - \Delta G_{CoPc}$ using the LANL2DZ basis set for Co, 6-31G(d,p) basis set for C, N, and H, and BP86-D3 functional. [b]For the C-PCM model, the radii used for molecular cavity generation are given in parentheses.

Supplemental Note on CoFPc/C Co(II/I) Redox

CoFPc/C displays a pH-independent reversible couple assigned to the Co(II/I) redox process at −0.12 V (**Figure S6**), but there is a marked scan rate and CoFPc loading dependence to the reversibility of this wave and its $E_{1/2}$ value (**Figures S7-9**). The couple is symmetrically reversible at scan rates of 100 mV s^{-1} or above. At slower scan rates, the reductive wave remains at the same peak potential, but the oxidative return wave shifts positively by 170 mV. Importantly, the peak intensity of both cathodic and anodic waves remains largely unchanged upon continual cycling within the potential region. This behavior is in line with an E_rC_i-E_rC_i cycle in which electrochemically reversible reductive electron transfer is coupled to an irreversible chemical step and return electrochemically reversible oxidation is also coupled to an irreversible chemical step that restores the original complex. The ability to outcompete this chemical step at scan rates as low as 100 mV s^{-1} suggests that the chemical step is relatively slow. We speculate that this chemical irreversibility results from motion of the molecule on the surface that results in a change in its adsorption site and/or orientation.

To probe whether CoFPc surface arrangement affects its observed redox properties, we employed films with much higher CoFPc loadings (approximately 37 nmol cm^{-2} versus the lower loadings 6-9 nmol cm^{-2}). For these high loading films, the reversible redox feature observed at 100 mV s^{-1} remains reversible at 5 mV s^{-1}, with the additional appearance of the same positively shifted oxidative wave seen for the films with low CoFPc loading (**Figure S9**). This suggests that the scan rate-dependent redox feature could correspond to more labile CoFPc adsorption sites which are saturated at high CoFPc loading, and the remainder of the CoFPc occupy sites that do not display any chemical irreversibility during the redox process. We note that the $E_{1/2}$ of the fully reversible redox wave observed at 100 mV s^{-1} is approximately 50 mV more negative for films with high CoFPc loading versus low CoFPc loading. This could also result from distinct adsorption behavior when greater amounts of CoFPc are present on the surface. Presuming that surface effects are less salient for higher loading films where many more molecules may be adsorbed to each other rather than the surface, we propose that the higher loading film $E_{1/2}$ reflects a less surface-perturbed Co(II/I) process. Thus, we use the $E_{1/2}$ of −0.17 V determined at 100 mV s^{-1} in the high CoFPc loading films to define the Co(II/I) redox potential for CoFPc/C (**Figure 2a**).

Supplemental Note on Stepwise PCET

Consider a hypothetical PCET pathway proceeding through a quasi-equilibrated ET followed by a rate-determining chemical step PT to the reduced catalyst $\mathbf{M}^{-}$ (**Figure S2b**). This constitutes an EC' sequence where the ET is quasi-equilibrated. In this scenario, we assume that adding electron-withdrawing substituents does not cause a change in bond dissociation free energy, *BDFE*, between two catalysts, meaning there is no change in the overall PCET thermochemistry (as we observed computationally for CoPc and CoFPc). This occurs when the change in $E_{1/2}$ of the Co(II/I) process is compensated by an opposing change in the pK_a of the Co–H. This is represented mathematically in **Equation 1** and rearranged in **Equation 2** with terms for Faraday's constant, *F*, gas constant, *R*, temperature, *T*, and 2.303 as the approximate value of the ln(10) factor.

$$\Delta BDFE = -\left(F\left(\Delta E_{1/2}\right) + 2.303RT(\Delta pK_a)\right) = 0 \tag{1}$$

$$\Delta pK_a = -\frac{F}{2.303RT}(\Delta E_{1/2}) \tag{2}$$

The Brønsted and Eyring-Evans-Polanyi relations[25–30] provide a description of the PT step barrier, $\Delta G^{\ddagger}_{PT}$, in **Equation 3** with the Brønsted α_{PT} scale factor and a constant *C*. The PT refers to formation of Co–H from Co(I), and the pK_a is that of the Co–H. Between the two catalysts, **Equation 4** correlates the difference in the barrier for the PT step, $\Delta\Delta G^{\ddagger}_{PT}$, to Δp$K_\mathrm{a}$. Using Equation 2, $\Delta\Delta G^{\ddagger}_{PT}$ can also be written in terms of $\Delta E_{1/2}$ and α_{PT}.

$$\Delta G^{\ddagger}_{PT} = -2.303RT(\alpha_{PT}pK_a) + C \tag{3}$$

$$\Delta\Delta G^{\ddagger}_{PT} = {\Delta G^{\ddagger}_{PT}}^{(2)} - {\Delta G^{\ddagger}_{PT}}^{(1)} = -2.303RT(\alpha_{PT}\Delta pK_a) = F(\alpha_{PT}\Delta E_{1/2}) \tag{4}$$

Equation 5 defines the overall reaction barrier, $\Delta G^{\ddagger}_{PCET}$, as a sum of the quasi-equilibrated ET step energy, $-F(\Delta E_{1/2})$, and the rate-determining PT step barrier, $\Delta G^{\ddagger}_{PT}$. Between the two catalysts, **Equation 6** correlates the difference in the overall reaction barrier, $\Delta\Delta G^{\ddagger}_{PCET}$, to contributions from $\Delta E_{1/2}$ and $\Delta\Delta G^{\ddagger}_{PT}$. **Equation 4** substitutes for $\Delta\Delta G^{\ddagger}_{PT}$. Simplifying the expression produces the $-F(1-\alpha_{PT})$ scale factor between $\Delta E_{1/2}$ and the difference in the overall reaction barrier shown in **Figure S2b** and **Figure 8a**.

$$\Delta G^{\ddagger}_{PCET} = -F(E_{1/2}) + \Delta G^{\ddagger}_{PT} \tag{5}$$

$$\Delta\Delta G^{\ddagger}_{PCET} = \Delta G^{\ddagger}_{PCET}{}^{(2)} - \Delta G^{\ddagger}_{PCET}{}^{(1)} = -F(\Delta E_{1/2}) + \Delta\Delta G^{\ddagger}_{PT} = -F(\Delta E_{1/2}) + F(\alpha_{PT}\Delta E_{1/2})$$
$$= -F(1-\alpha_{PT})(\Delta E_{1/2}) \qquad \textbf{(6)}$$

Figure S2a illustrates simulated Tafel plots for HER catalysis with the rate-determining PCET step described by **Figure S2b-c**. For each catalyst, quasi-equilibrated ET followed by rate-determining PT prescribes an ideal Tafel slope of −59 mV dec^{-1} until *E* reaches $E_{1/2}$ (described by **Figure S2b** and **Equations 1-6**). When *E* is more negative than $E_{1/2}$, the rate plateaus at the log of the maximum rate constant of catalysis, log(k_{cat}) (described by **Figure S2c** and **Equations 1-4**).[31,32]

To derive the role of $\Delta E_{1/2}$ in defining PCET rates between the two catalysts, we use the Eyring-Evans-Polanyi relations to relate the difference in the log of the apparent rate constant, log(k_{app}), to the difference in the overall reaction barrier (**Equation 7**).

$$\Delta\log(k_{app}) = -\frac{1}{2.303RT}(\Delta\Delta G^{\ddagger}_{PCET}) \qquad \textbf{(7)}$$

The plateau region is caused by the ET step becoming downhill in energy (**Figure S2c**). This is because applying *E* more negative than $E_{1/2}$ causes the energy of the initial reactant state to rise above the energy of the reduced intermediate state. This removes the ability of *E* to affect the overall reaction barrier and thus, when both catalysts are in the plateau region, the difference in overall reaction barriers simplifies to the difference in PT reaction barriers (**Equation 8**).

$$\Delta\Delta G^{\ddagger}_{PCET} = \Delta\Delta G^{\ddagger}_{PT} \qquad \text{(in the rate plateau)} \ \textbf{(8)}$$

We combine **Equations 4**, **7**, and **8** to produce **Equation 9** describing the relationship between $\Delta E_{1/2}$ and the log of the apparent rate constant of catalysis at the plateau, log($k_{app,max}$), which is commonly termed the log of the maximum rate constant of catalysis, log(k_{cat}).

$$\Delta\log(k_{app,max}) = \Delta\log(k_{cat}) = -\frac{1}{2.303RT}(\Delta\Delta G^{\ddagger}_{PT}) = -\frac{F}{2.303RT}(\alpha_{PT}\Delta E_{1/2}) \quad \text{(in the rate plateau)} \ \textbf{(9)}$$

The room temperature value of −2.303*RT*/*F* is approximately −59 mV. Thus, **Equation 9** returns that an α_{PT} value of 1 results in the plateau rate decreasing by one order of magnitude with every 59 mV increase in $E_{1/2}$. Sub-unity values of α_{PT} describe a shallower slope; for example, an α_{PT} value of 0.5 means the plateau rate decreases by one order of magnitude with every 118 mV increase in $E_{1/2}$ (less negative $E_{1/2}$ for this reductive PCET process).

In the −59 mV dec^{-1} sloped region of the Tafel plot for both catalysts, we combine **Equations 6** and **7** to produce **Equation 10** relating $\Delta E_{1/2}$ and the log of the apparent rate constant of catalysis.

$$\Delta\log(k_{app}) = -\frac{1}{2.303RT}(\Delta\Delta G^{\ddagger}_{PCET}) = \frac{F}{2.303RT}(1-\alpha_{PT})(\Delta E_{1/2}) \quad \text{(in the sloped region)} \ \textbf{(10)}$$

Equation 10 returns that an α_{PT} value of 1 results in the sloped region of the Tafel plot being insensitive to changes in $E_{1/2}$. However, sub-unity values of α_{PT} cause the rates in the sloped region to separate based on $\Delta E_{1/2}$; for example, an α_{PT} value of 0.5 means the sloped region rate increases by one order of magnitude with every 118 mV increase in $E_{1/2}$ (less negative $E_{1/2}$ for this reductive PCET process). Note that this is the opposite of the trend for sub-unity α_{PT} in the plateau region.

Critically, in all regions of the Tafel plot, a sub-unity value of α_{PT}, which is most commonly the case, returns a difference in PCET rates based on a difference in $E_{1/2}$, despite identical overall PCET thermochemistry. (There is one E value between both $E_{1/2}$ where rates should overlap, but varying E around this value should cause rates to diverge again).

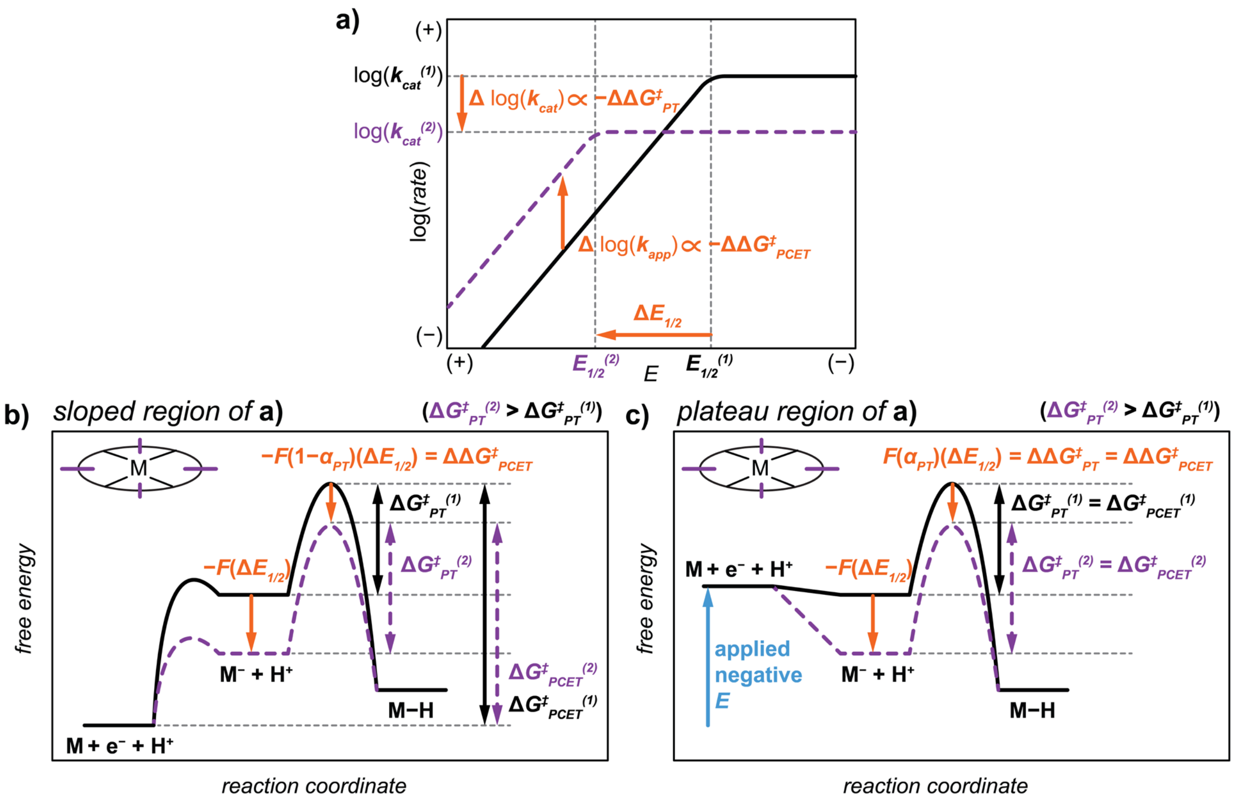

Figure S2. a) Simulated Tafel plots for HER catalysis with its rate-determining PCET step described by panel **b**, which prescribes ideal Tafel slopes of −59 mV dec^{-1} until the rate plateaus beyond $E_{1/2}$. **b)** Stepwise ET-PT diagram from main text **Figure 8a** for two molecules with the same *BDFE*, in an applied E regime less negative than either $E_{1/2}$. Equations 1-6 derive the scale factor $-F(1-\alpha_{PT})$ governing the sloped region of panel **a**. **c)** The same stepwise ET-PT diagram is shown in an applied E regime more negative than either $E_{1/2}$ such that the ET step becomes downhill in energy. Equations 1-4 and 8 derive the simplified scale factor $F(\alpha_{PT})$ governing the plateau region of panel **a**.

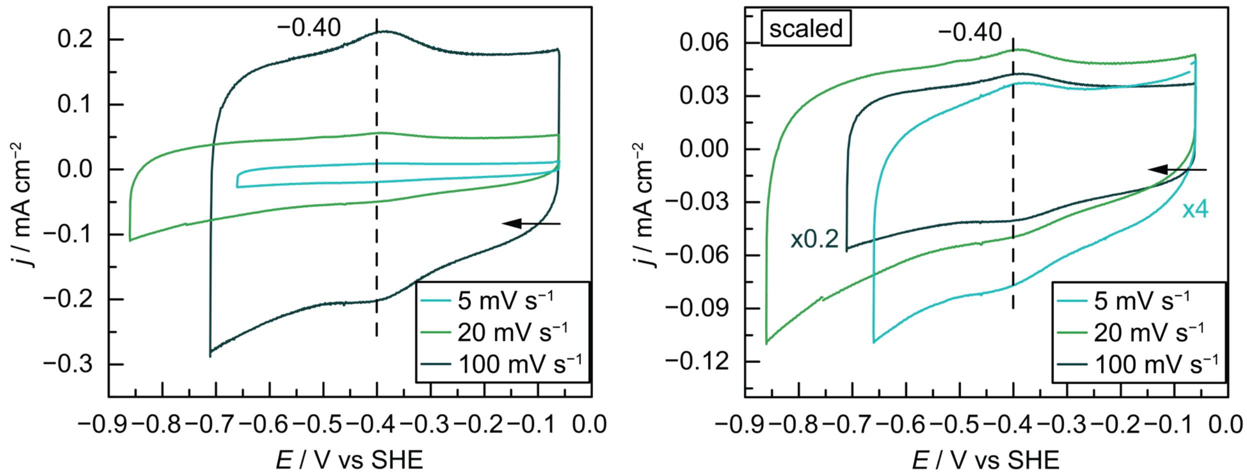

Figure S3. Scan rate dependence of the Co(II/I) redox couple for CoPc/C. The ICP-MS measured Co loading for this film is 4.1 nmol cm^{-2}. The right panel shows the same data with currents scaled as indicated for easier visual comparison of the redox feature.

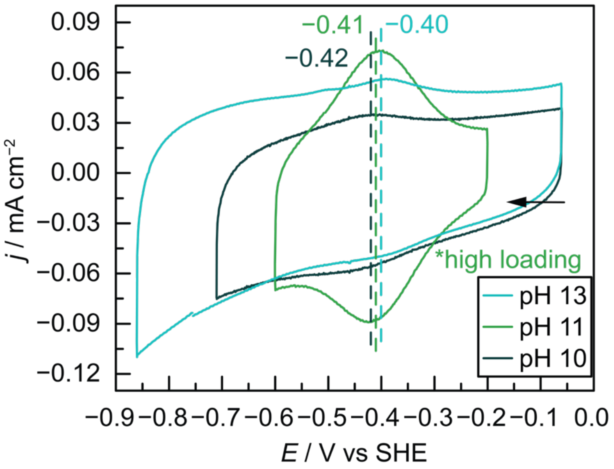

Figure S4. pH dependence of the Co(II/I) redox couple for CoPc/C recorded in 0.1 M NaOH (pH 13) and Britton-Robinson buffers (pH 11 and pH 10). The voltammograms were recorded with a scan rate of 20 mV s^{-1}. The pH 13 and pH 10 data were collected on films with ICP-MS measured Co loadings of 4.1 and 3.5 nmol cm^{-2}, respectively, while the pH 11 data were collected on a different film of nominal 80 nmol cm^{-2} CoPc loading.

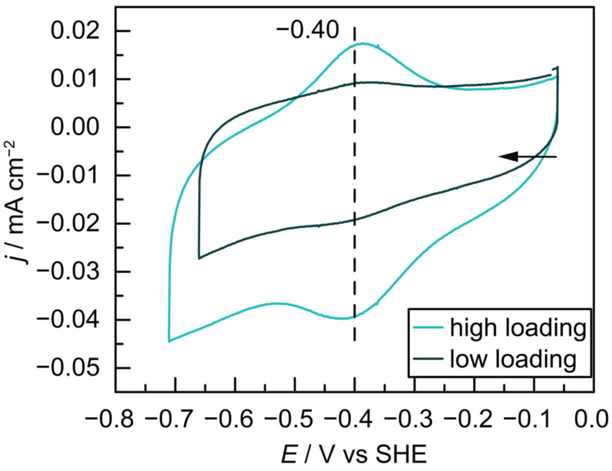

Figure S5. Catalyst loading dependence of the Co(II/I) redox couple for CoPc/C. The voltammograms were recorded with a scan rate of 5 mV s^{-1}. The ICP-MS measured Co loading is 71 nmol cm^{-2} for the high loading film and 4.1 nmol cm^{-2} for the low loading film.

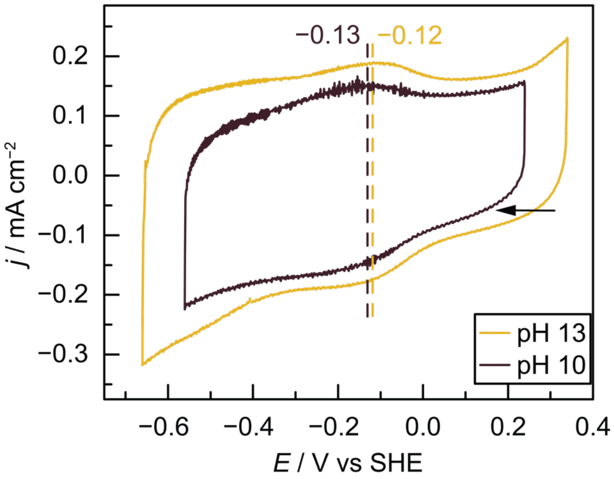

Figure S6. pH dependence of the Co(II/I) redox couple for CoFPc/C recorded in 0.1 M NaOH (pH 13) and Britton-Robinson buffer (pH 10). The voltammograms were recorded with a scan rate of 100 mV s^{-1}. The pH 13 data were collected on a film of nominal 5.9 nmol cm^{-2} CoFPc loading, and the pH 10 data were collected on a film with ICP-MS measured Co loading of 4.4 nmol cm^{-2}.

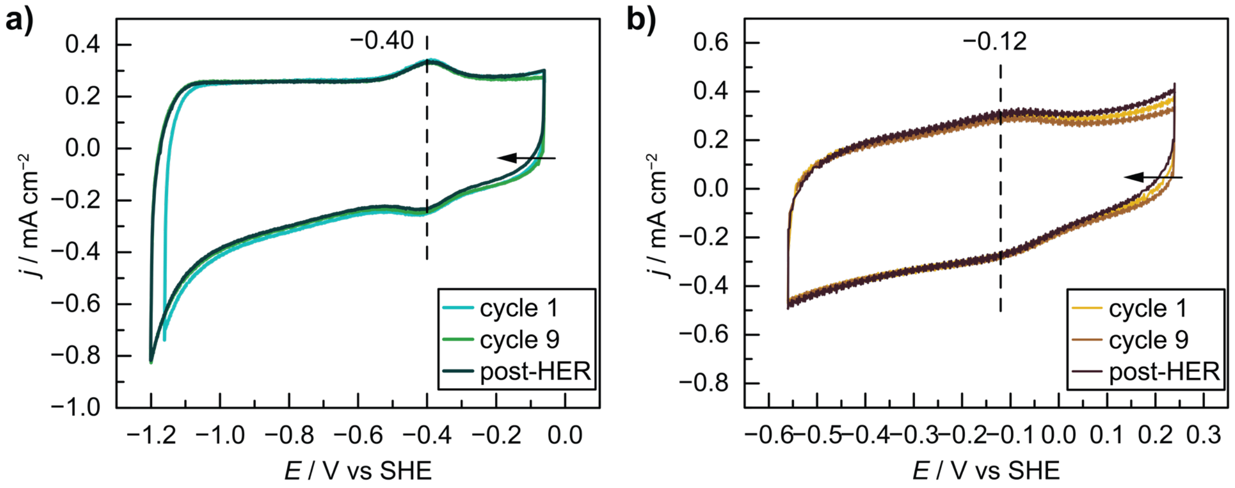

Figure S7. Stability of the Co(II/I) redox couple over 9 cycles and after 20 min HER electrolysis at −1.23 V vs. SHE for **a)** CoPc/C, recorded with a scan rate of 100 mV s^{-1}; **b)** CoFPc/C, recorded with a scan rate of 300 mV s^{-1}.

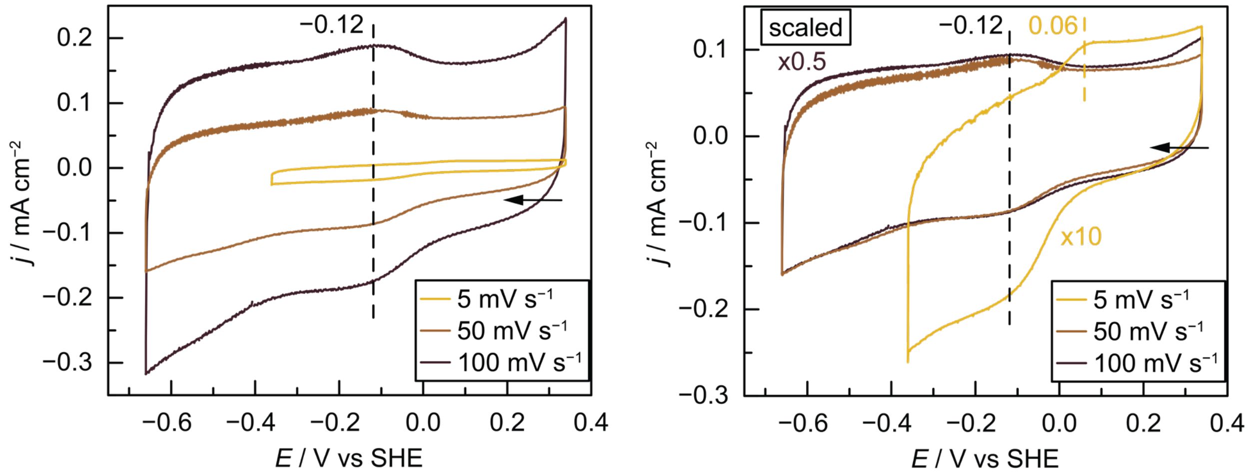

Figure S8. Scan rate dependence of the Co(II/I) redox couple for CoFPc/C. This film has a nominal 5.9 nmol cm^{-2} CoFPc loading. The right panel shows the same data with currents scaled as indicated for easier visual comparison of the redox feature.

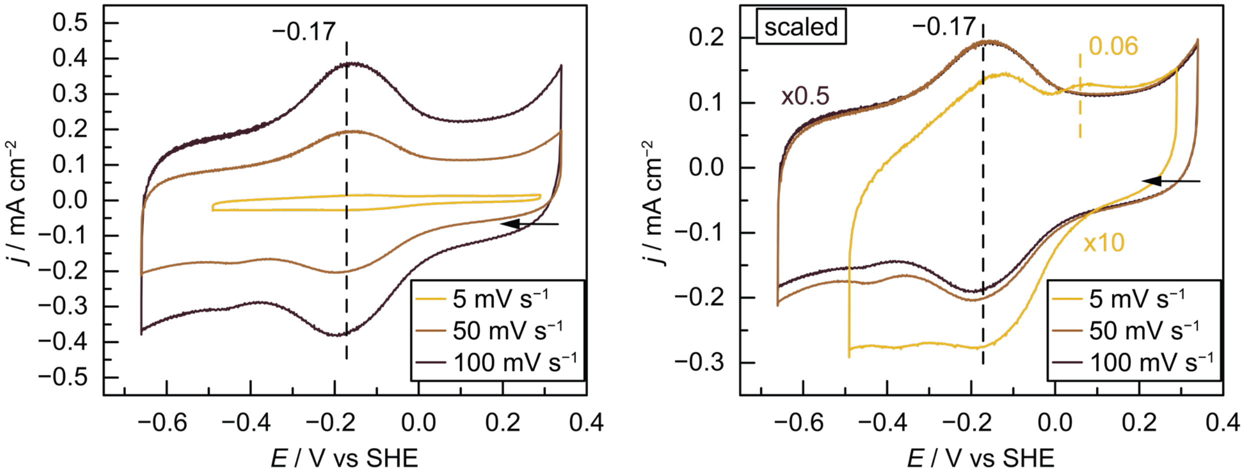

Figure S9. Scan rate dependence of the Co(II/I) redox couple for CoFPc/C. This film has a nominal 42 nmol cm^{-2} CoFPc loading. The right panel shows the same data with currents scaled as indicated for easier visual comparison of the redox feature.

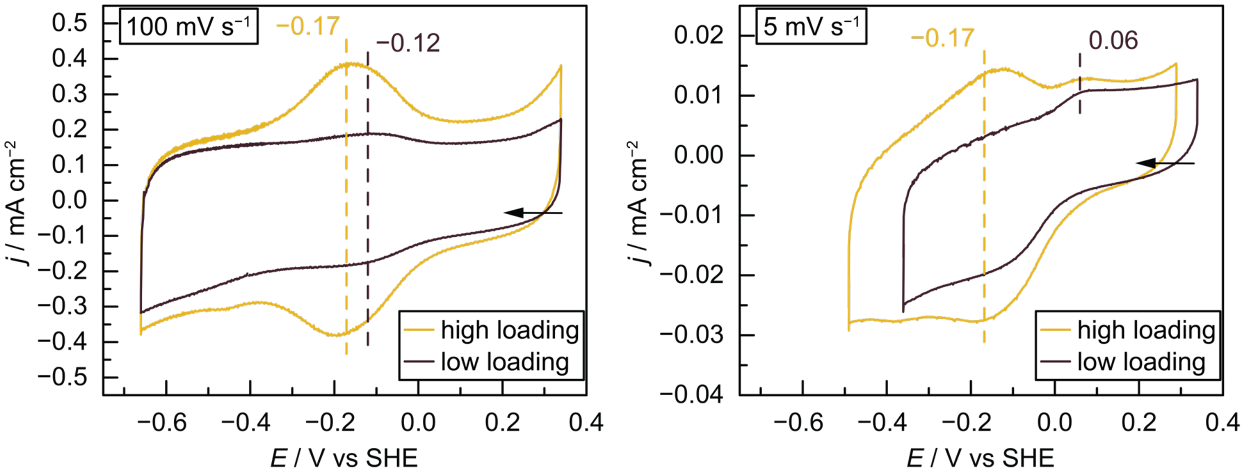

Figure S10. Catalyst loading dependence of the Co(II/I) redox couple for CoFPc/C. The nominal CoFPc loading is 42 nmol cm^{-2} for the high loading film and 5.1 nmol cm^{-2} for the low loading film. The two panels correspond to data collected at two different scan rates.

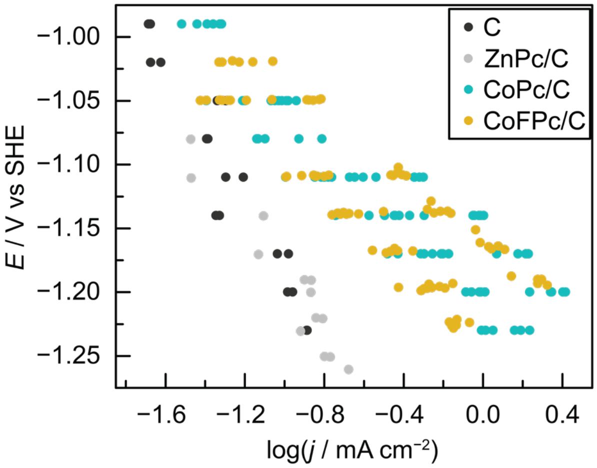

Figure S11. Steady-state HER Tafel data from two unmodified C films and two ZnPc/C films collected via a random series of applied potentials. All of the CoPc/C and CoFPc/C film data from **Figures S14** and **S15** are overlaid for comparison.

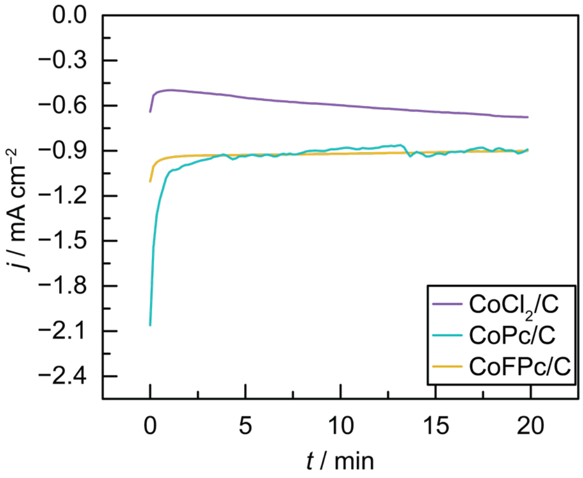

Figure S12. HER CA trace at −1.23 V vs SHE for CoPc/C, CoFPc/C, and $CoCl_2$/C recorded over approximately 20 min. The ICP-MS measured Co loadings are 4.1 nmol cm^{-2} CoPc, 4.9 nmol cm^{-2} CoFPc, and 7.2 nmol cm^{-2} $CoCl_2$.

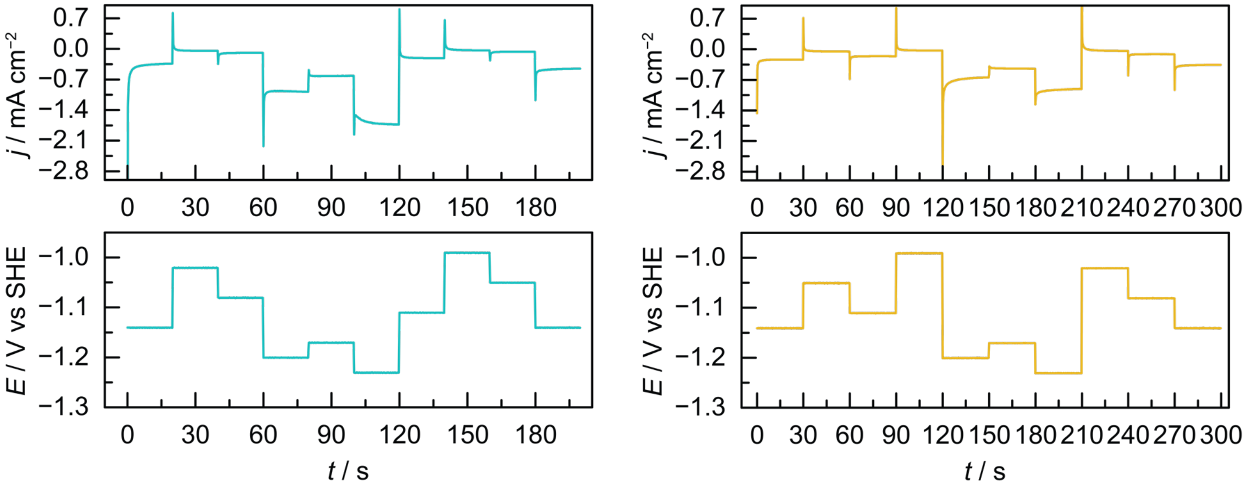

Figure S13. Representative examples of a random CA sequence of applied *E* (both sides, bottom) and corresponding measured *j* for CoPc/C (left side, top) and CoFPc/C (right side, top). The ICP-MS measured Co loadings of these two films are 4.9 and 8.5 nmol cm^{-2}, respectively.

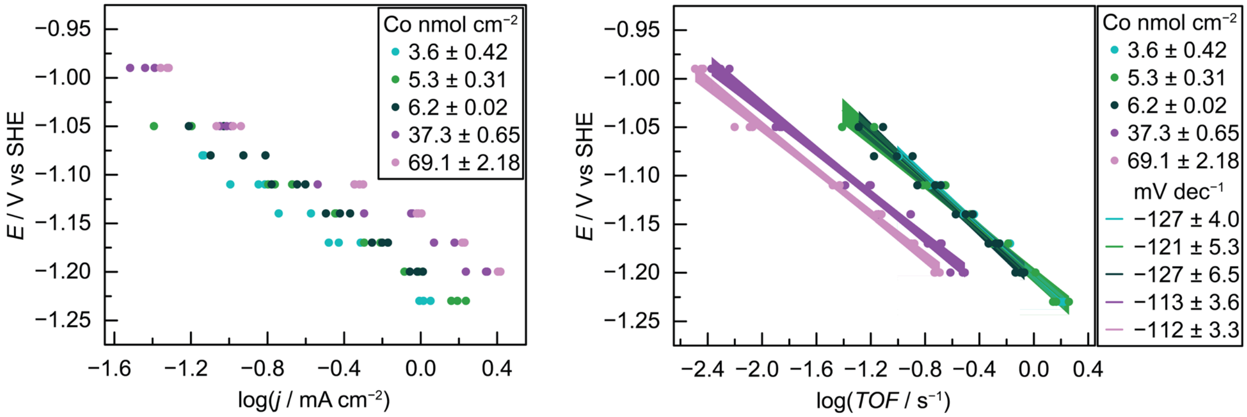

Figure S14. Steady-state HER Tafel data from CoPc/C films of various catalyst loadings collected via a random series of applied potentials. The data from each of 15 films are plotted independently. The loading groups noted in the legend correspond to 3 films each. The film Co loadings are derived from ICP-MS measurement. The right panel converts the left panel log(*j*) into log(*TOF*) for each independent film using its measured loading. The solid lines represent linear fits of each loading group (3 films) with the slopes and errors noted in the legend. The shaded regions correspond to a 95% confidence interval around each linear fit. These linear fits from the unaggregated data are used in main text **Figure 3** shown alongside the triplicate averaged data points.

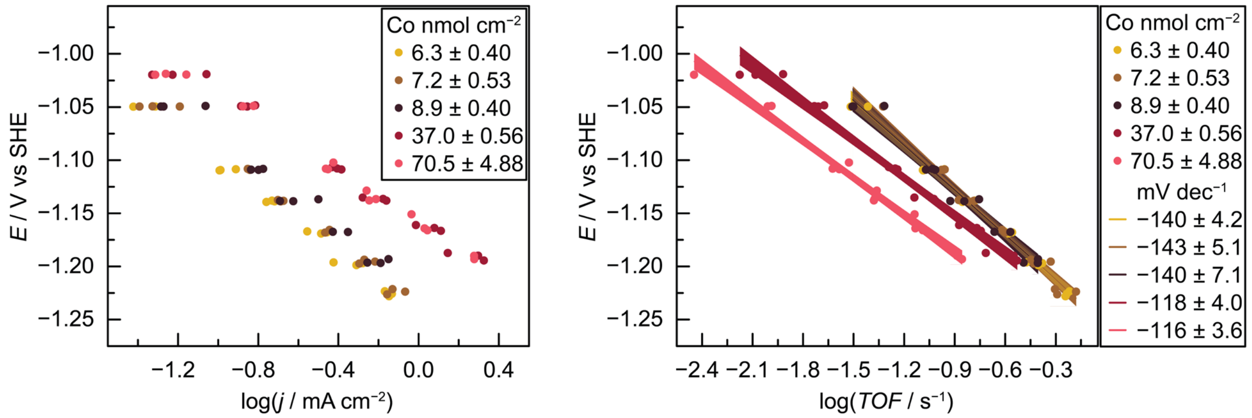

Figure S15. Steady-state HER Tafel data from CoFPc/C films of various catalyst loadings collected via a random series of applied potentials. The data from each of 15 films are plotted independently. The loading groups noted in the legend correspond to 3 films each. The film Co loadings are derived from ICP-MS measurement. The right panel converts the left panel log(j) into log(TOF) for each independent film using its measured loading. The solid lines represent linear fits of each loading group (3 films) with the slopes and errors noted in the legend. The shaded regions correspond to a 95% confidence interval around each linear fit. These linear fits from the unaggregated data are used in main text **Figure 3** shown alongside the triplicate averaged data points.

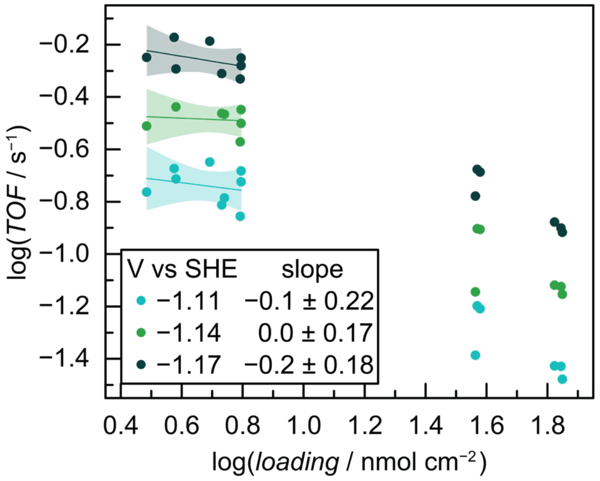

Figure S16. The same CoPc/C data from **Figure S14** are represented as log(TOF) vs log($loading$) at 3 different E values. The data below 0.9 units of log($loading$) are analyzed by linear fit (solid lines) with the slopes and errors noted in the legend. The shaded regions correspond to a 95% confidence interval around each linear fit.

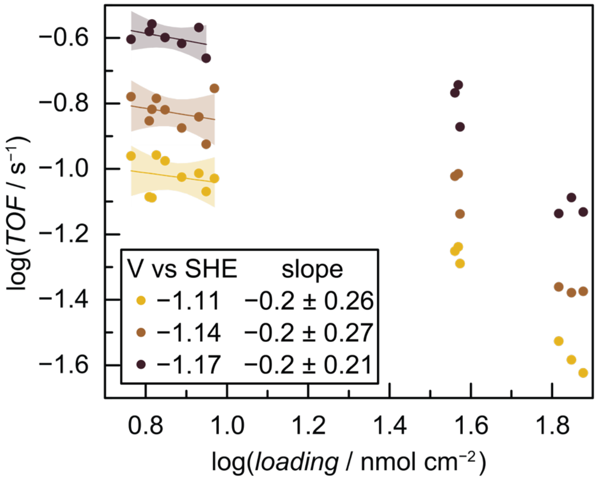

Figure S17. The same CoFPc/C data from **Figure S15** are represented as log(*TOF*) vs log(*loading*) at 3 different *E* values. The data below 1.1 units of log(*loading*) are analyzed by linear fit (solid lines) with the slopes and errors noted in the legend. The shaded regions correspond to a 95% confidence interval around each linear fit.

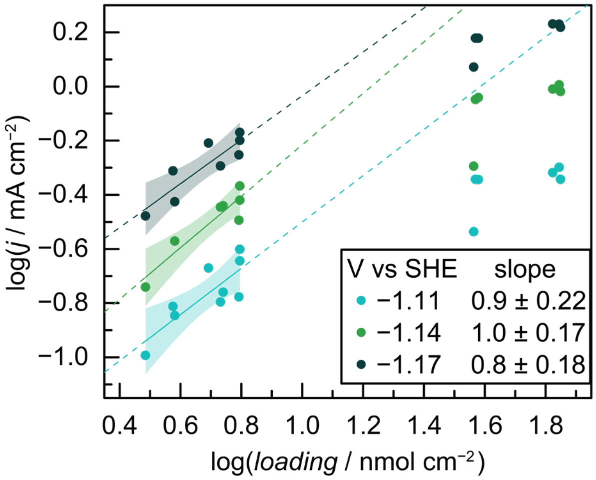

Figure S18. The same CoPc/C data from **Figure S14** are represented as log(*j*) vs log(*loading*) at 3 different *E* values. The data below 0.9 units of log(*loading*) are analyzed by linear fit (solid lines) with the slopes and errors noted in the legend. The shaded regions correspond to a 95% confidence interval around each linear fit. The dashed lines extrapolate the linear fits across the entire data range.

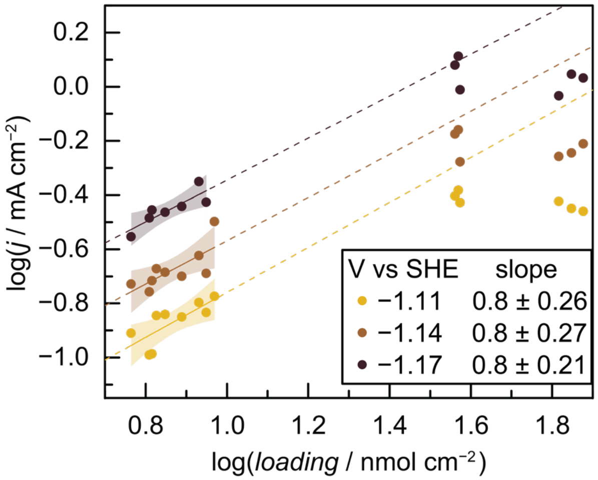

Figure S19. The same CoFPc/C data from **Figure S15** are represented as log(*j*) vs log(*loading*) at 3 different *E* values. The data below 1.1 units of log(*loading*) are analyzed by linear fit (solid lines) with the slopes and errors noted in the legend. The shaded regions correspond to a 95% confidence interval around each linear fit. The dashed lines extrapolate the linear fits across the entire data range.

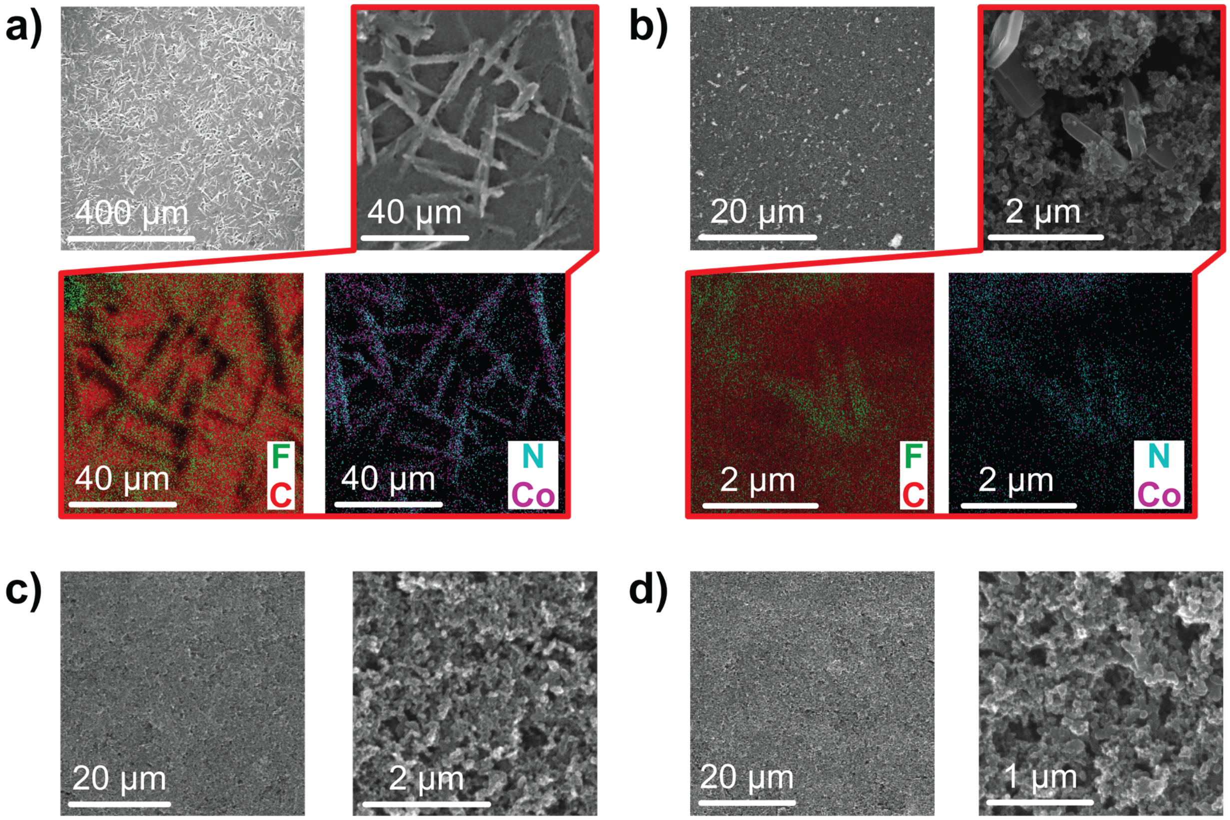

Figure S20. a) SEM-EDS of a CoPc/C film of nominal 80 nmol cm^{-2} CoPc loading. The top left EM image shows ~1% of the total film surface, while the top right image zooms in on a partial region. The bottom two images are the EDS spatial spectra of C, F, N, and Co corresponding to the top right region. **b)** SEM-EDS of a CoFPc/C film of nominal 77 nmol cm^{-2} CoFPc loading. The top left EM image shows ~0.1% of the total film surface, while the top right image zooms in on a partial region. The bottom two images are the EDS spatial spectra of C, F, N, and Co corresponding to the top right region. **c)** SEM of CoPc/C film of nominal 4.5 nmol cm^{-2} CoPc loading at two different magnifications. **d)** SEM of CoFPc/C film of nominal 8.3 nmol cm^{-2} CoFPc loading at two different magnifications.

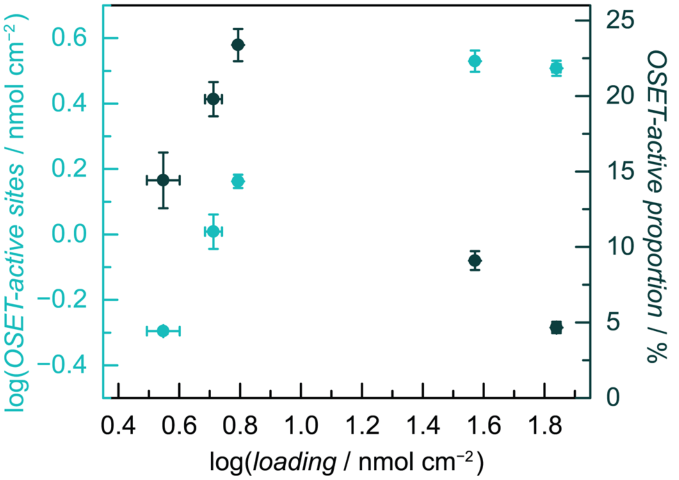

Figure S21. Co(II/I) OSET-active population of CoPc/C films of various catalyst loadings plotted versus their ICP-MS measured Co loadings. The left *y*-axis (blue) shows absolute OSET-active nmol cm^{-2} while the right *y*-axis (dark blue) shows OSET-active nmol cm^{-2} as a percentage of the *x*-axis ICP-MS nmol cm^{-2}.

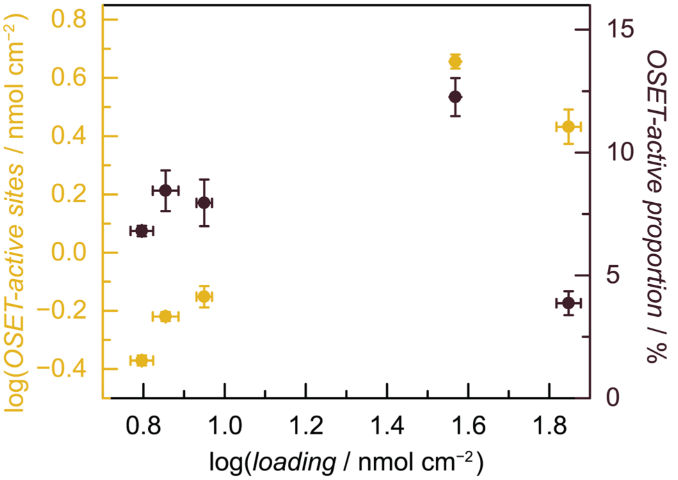

Figure S22. Co(II/I) OSET-active population of CoFPc/C films of various catalyst loadings plotted versus their ICP-MS measured Co loadings. The left *y*-axis (yellow) shows absolute OSET-active nmol cm^{-2} while the right *y*-axis (dark brown) shows OSET-active nmol cm^{-2} as a percentage of the *x*-axis ICP-MS nmol cm^{-2}.

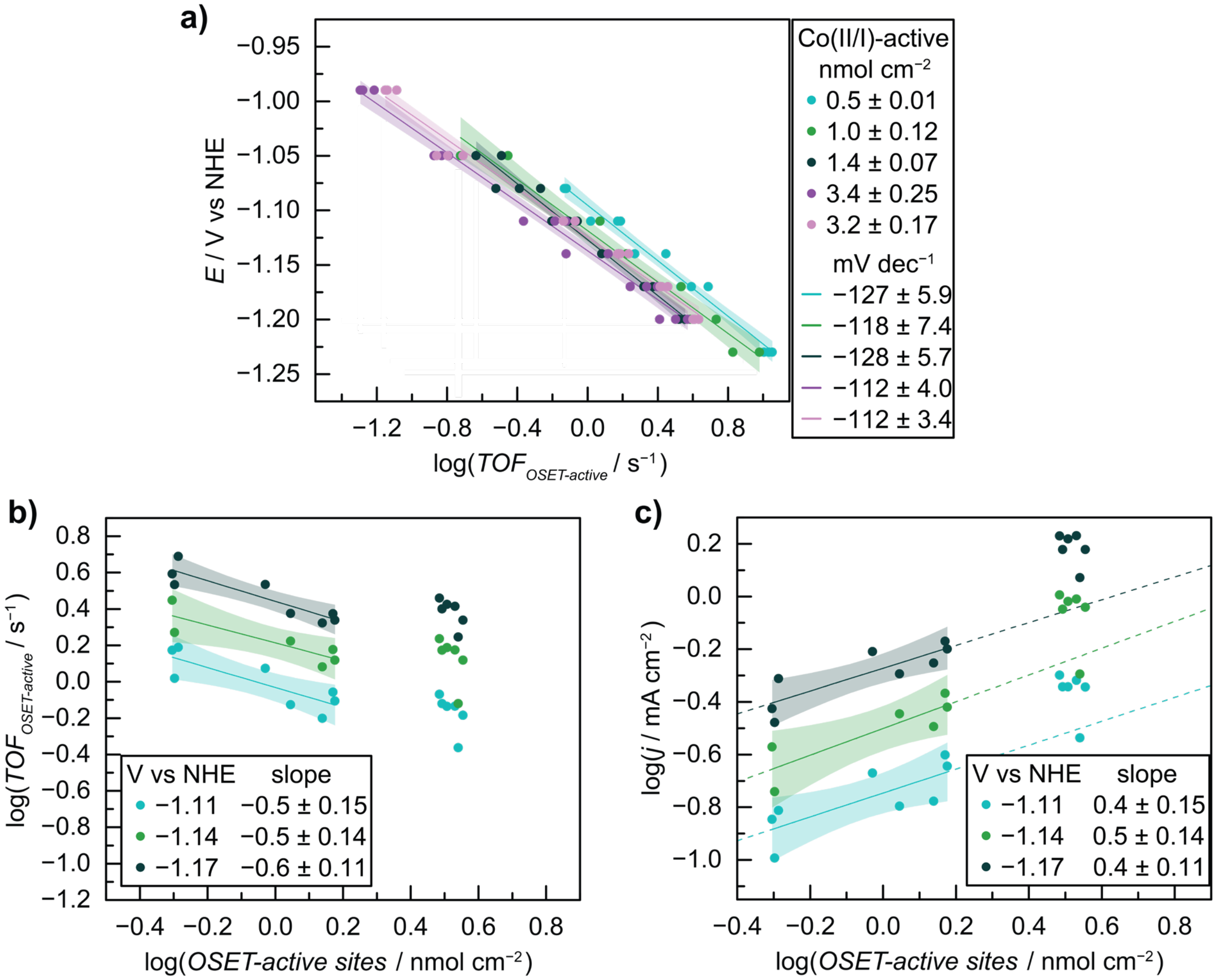

Figure S23. HER loading dependence for CoPc/C based on Co(II/I) OSET-active loading obtained by integration of the voltammetric wave. **a)** *E* vs log($TOF_{OSET\text{-}active\ sites}$) for each independent film. The solid lines represent linear fits of each loading group (3 films) with the slopes and errors noted in the legend. The shaded regions correspond to a 95% confidence interval around each linear fit. **b)** log($TOF_{OSET\text{-}active\ sites}$) vs log(*OSET-active sites*) at 3 different *E* values. The data below 0.3 units of log(*OSET-active sites*) are analyzed by linear fit (solid lines) with the slopes and errors noted in the legend. The shaded regions correspond to a 95% confidence interval around each linear fit. **c)** log(*j*) vs log(*OSET-active sites*) at 3 different *E* values. The data below 0.3 units of log(*OSET-active sites*) are analyzed by linear fit (solid lines) with the slopes and errors noted in the legend. The shaded regions correspond to a 95% confidence interval around each linear fit. The dashed lines extrapolate the linear fits across the entire data range.

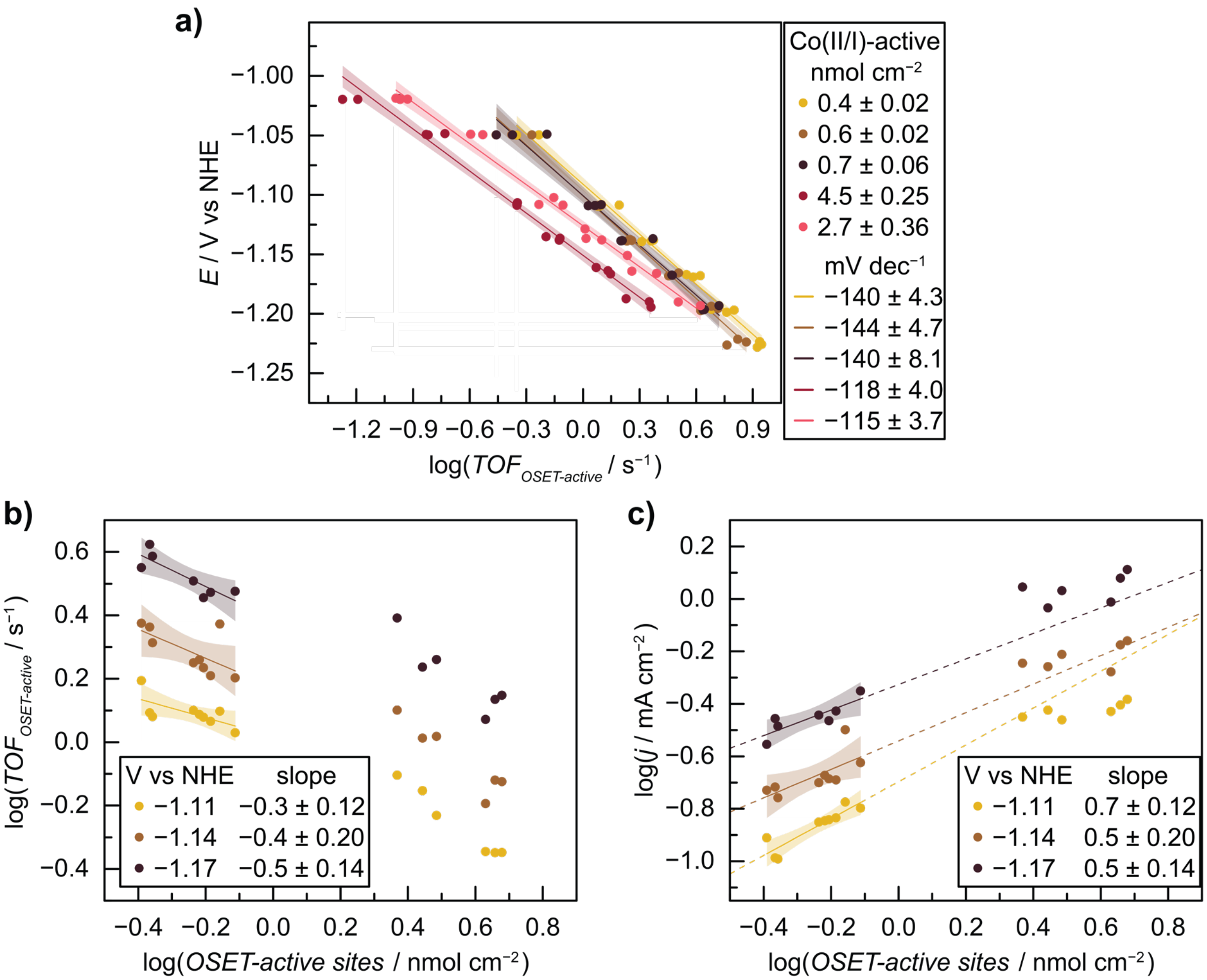

Figure S24. HER loading dependence for CoFPc/C based on Co(II/I) OSET-active loading obtained by integration of the voltammetric wave. **a)** E vs log($TOF_{OSET\text{-}active\ sites}$) for each independent film. The solid lines represent linear fits of each loading group (3 films) with the slopes and errors noted in the legend. The shaded regions correspond to a 95% confidence interval around each linear fit. **b)** log($TOF_{OSET\text{-}active\ sites}$) vs log(*OSET-active sites*) at 3 different E values. The data below 0 units of log(*OSET-active sites*) are analyzed by linear fit (solid lines) with the slopes and errors noted in the legend. The shaded regions correspond to a 95% confidence interval around each linear fit. **c)** log(j) vs log(*OSET-active sites*) at 3 different E values. The data below 0 units of log(*OSET-active sites*) are analyzed by linear fit (solid lines) with the slopes and errors noted in the legend. The shaded regions correspond to a 95% confidence interval around each linear fit. The dashed lines extrapolate the linear fits across the entire data range.

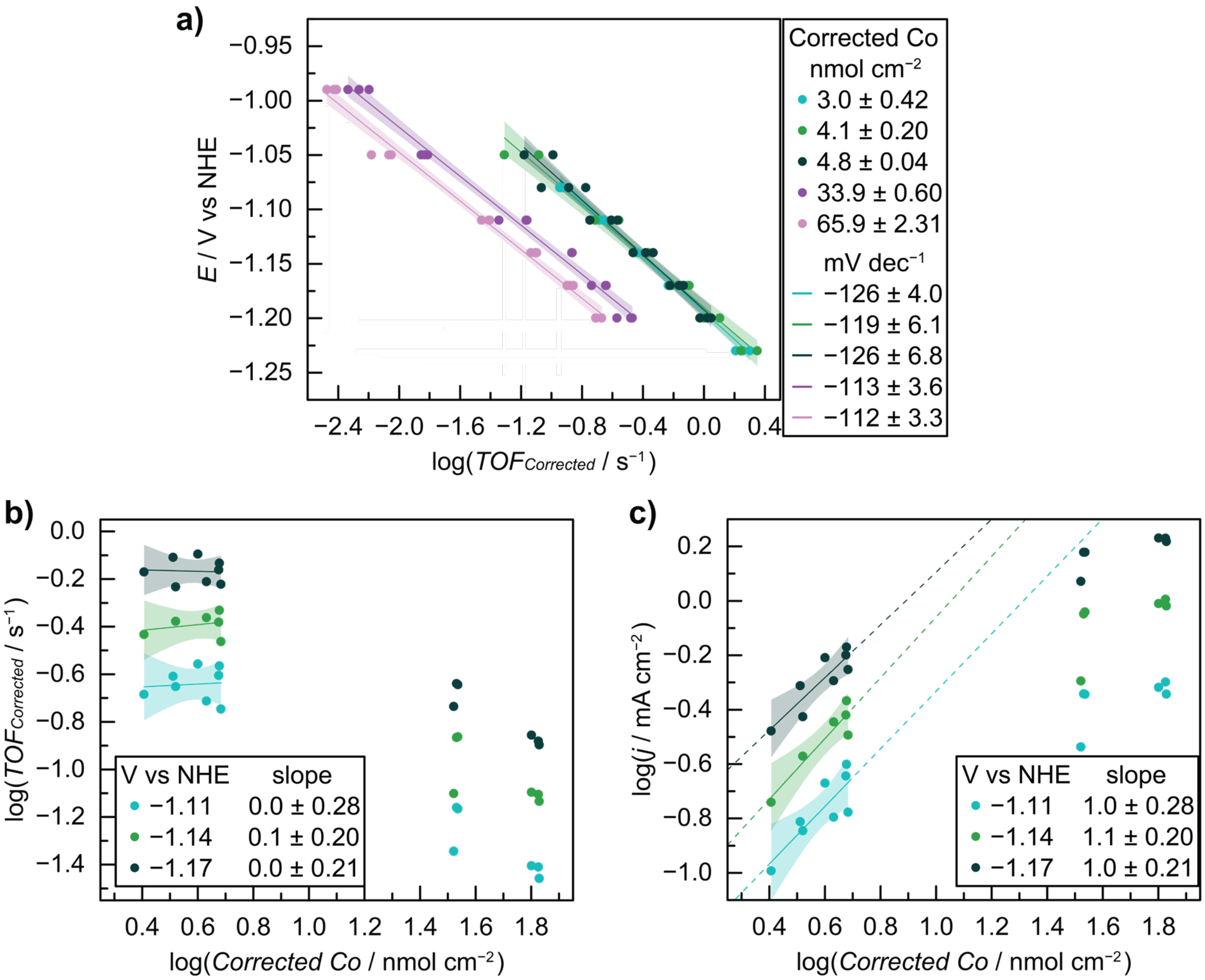

Figure S25. HER loading dependence for CoPc/C based on ICP-MS total Co loading minus the Co(II/I) OSET-active loading from integration of the voltammetric wave. **a)** E vs log($TOF_{Corrected}$) for each independent film. The solid lines represent linear fits of each loading group (3 films) with the slopes and errors noted in the legend. The shaded regions correspond to a 95% confidence interval around each linear fit. **b)** log($TOF_{Corrected}$) vs log(*Corrected Co*) at 3 different E values. The data below 0.8 units of log(*Corrected Co*) are analyzed by linear fit (solid lines) with the slopes and errors noted in the legend. The shaded regions correspond to a 95% confidence interval around each linear fit. **c)** log(j) vs log(*Corrected Co*) at 3 different E values. The data below 0.8 units of log(*Corrected Co*) are analyzed by linear fit (solid lines) with the slopes and errors noted in the legend. The shaded regions correspond to a 95% confidence interval around each linear fit. The dashed lines extrapolate the linear fits across the entire data range.

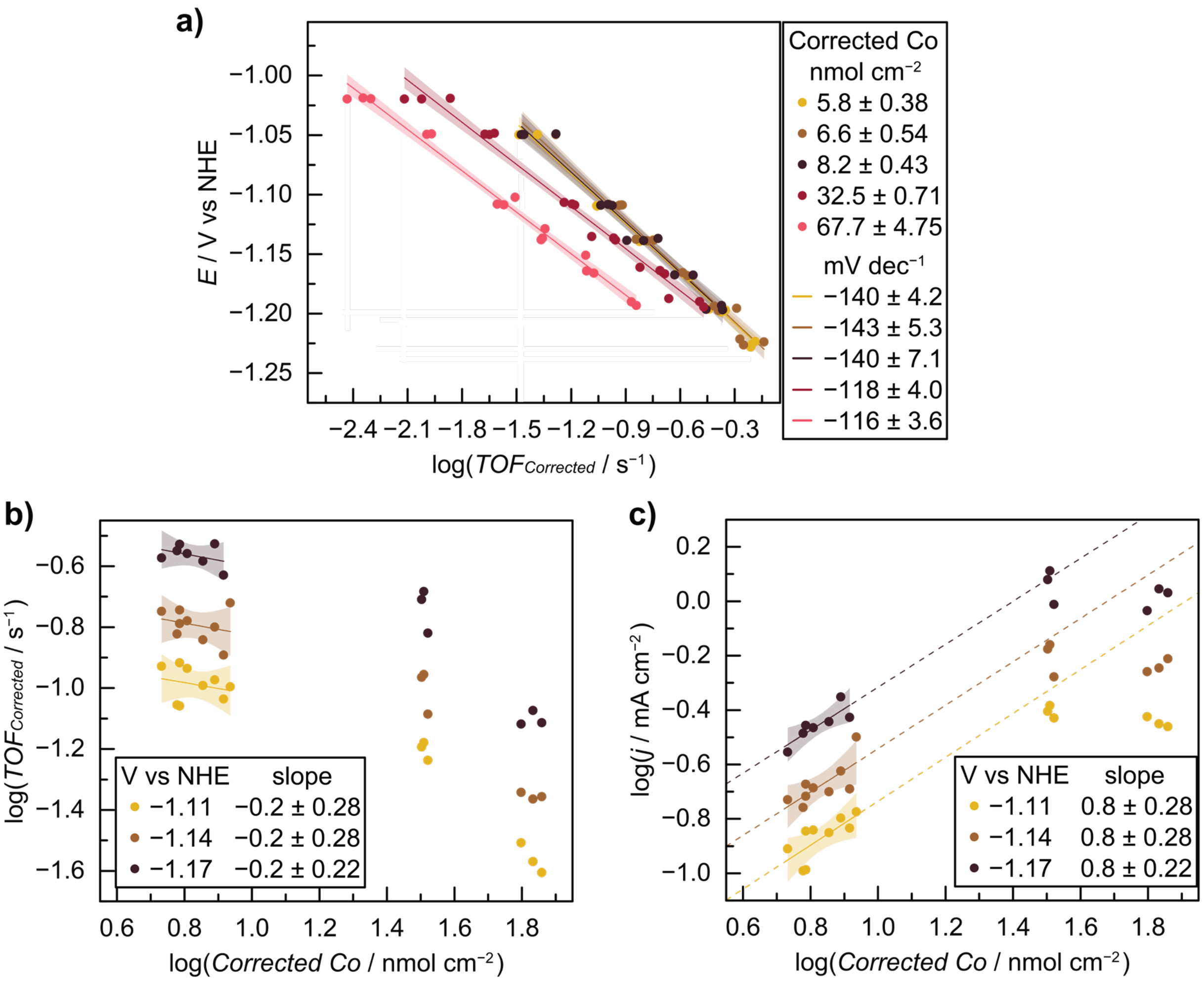

Figure S26. HER loading dependence for CoFPc/C based on ICP-MS total Co loading minus the Co(II/I) OSET-active loading from integration of the voltammetric wave. **a)** E vs log($TOF_{Corrected}$) for each independent film. The solid lines represent linear fits of each loading group (3 films) with the slopes and errors noted in the legend. The shaded regions correspond to a 95% confidence interval around each linear fit. **b)** log($TOF_{Corrected}$) vs log(*Corrected Co*) at 3 different E values. The data below 1.0 units of log(*Corrected Co*) are analyzed by linear fit (solid lines) with the slopes and errors noted in the legend. The shaded regions correspond to a 95% confidence interval around each linear fit. **c)** log(j) vs log(*Corrected Co*) at 3 different E values. The data below 1.0 units of log(*Corrected Co*) are analyzed by linear fit (solid lines) with the slopes and errors noted in the legend. The shaded regions correspond to a 95% confidence interval around each linear fit. The dashed lines extrapolate the linear fits across the entire data range.

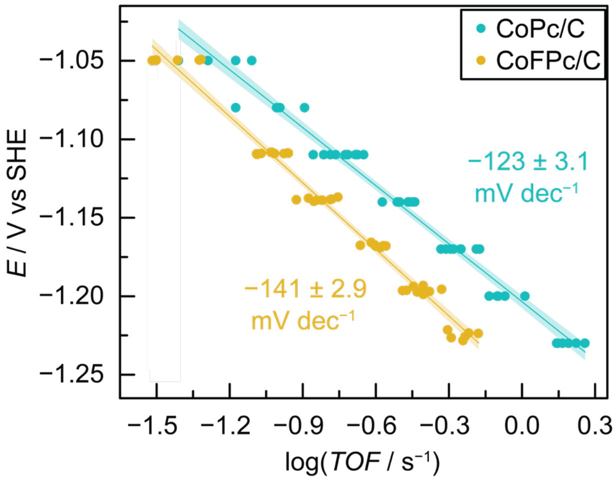

Figure S27. The low catalyst loading site-normalized Tafel data from **Figures S14** and **S15** are shown here to compare CoPc/C and CoFPc/C. The 9 films of each MME type are analyzed by linear fit (solid lines) with the slopes and errors noted beside. The shaded regions correspond to a 95% confidence interval around each linear fit. These linear fits from the unaggregated data are used in main text **Figure 4** shown alongside the averaged data points from the nine replicates shown here.

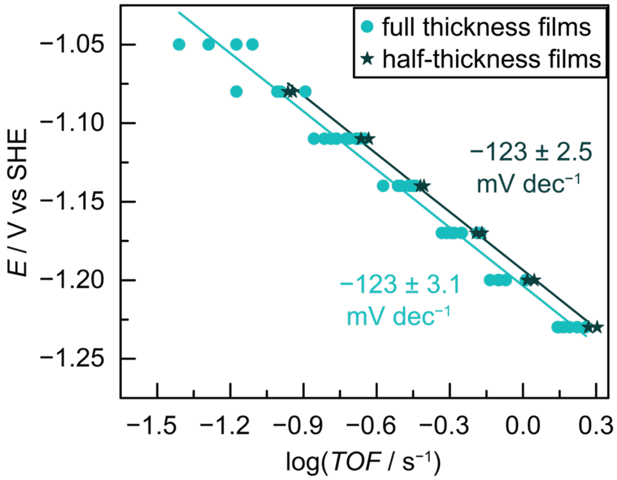

Figure S28. Steady-state HER Tafel data from 2 half-thickness CoPc/C films collected via a random series of applied potentials. The data have been site-normalized using the ICP-MS measured Co loading of each film. The CoPc/C data from **Figure S27** is included for comparison. The solid lines represent linear fits with the slopes and errors noted beside.

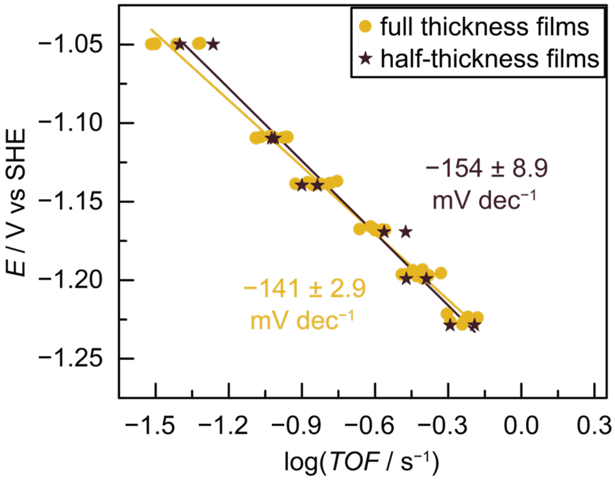

Figure S29. Steady-state HER Tafel data from 2 half-thickness CoFPc/C films collected via a random series of applied potentials. The data have been site-normalized using the ICP-MS measured Co loading of each film. The CoFPc/C data from **Figure S27** is included for comparison. The solid lines represent linear fits with the slopes and errors noted beside.

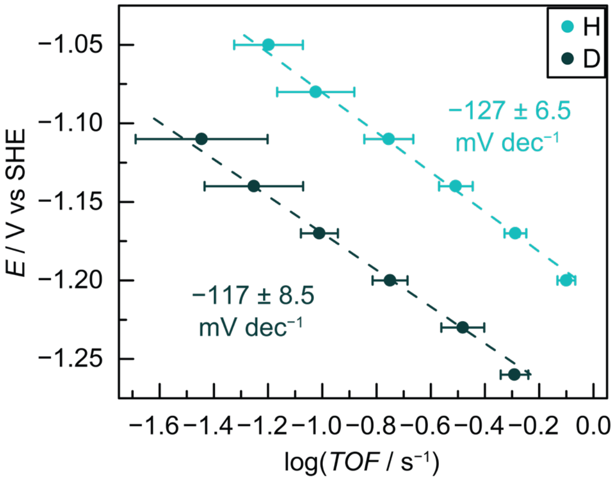

Figure S30. Steady-state HER Tafel data from CoPc/C films collected via a random series of applied potentials in 0.1 M NaOH in H_2O (blue) or 0.1 M NaOH in D_2O (dark blue). Averaged data of 3 films are shown for each condition, with ICP-MS measured Co loading of 6.2 ±0.02 nmol cm^{-2} in H_2O and 6.5 ±0.51 nmol cm^{-2} in D_2O. The dashed lines represent linear fits of the unaggregated film data (not shown) with the slopes and errors noted beside.

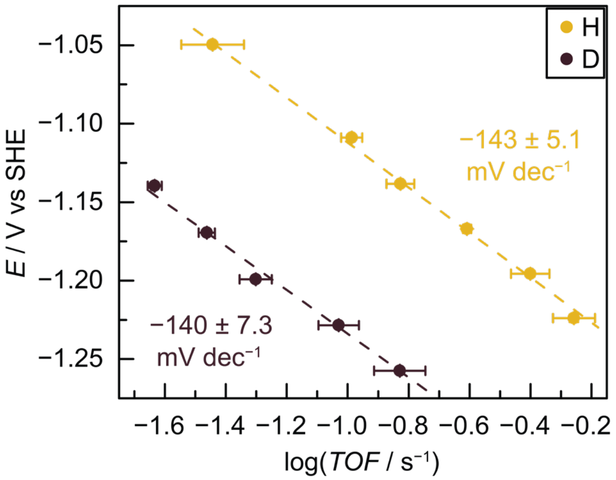

Figure S31. Steady-state HER Tafel data from CoFPc/C films collected via a random series of applied potentials in 0.1 M NaOH in H_2O (yellow) or 0.1 M NaOH in D_2O (dark brown). Averaged data of 3 films are shown for each condition, with ICP-MS measured Co loading of 7.2 ±0.53 nmol cm^{-2} in H_2O and 7.4 ±0.38 nmol cm^{-2} in D_2O. The dashed lines represent linear fits of the unaggregated film data (not shown) with the slopes and errors noted beside.

References

(1) Frisch, M. J.; Trucks, G. W.; Schlegel, H. B.; Scuseria, G. E.; Robb, M. A.; Cheeseman, J. R.; Scalmani, G.; Barone, V.; Petersson, G. A.; Nakatsuji, H.; Li, X.; Caricato, M.; Marenich, A. V.; Bloino, J.; Janesko, B. G.; Gomperts, R.; Mennucci, B.; Hratchian, H. P.; Ortiz, J. V.; Izmaylov, A. F.; Sonnenberg, J. L.; Williams; Ding, F.; Lipparini, F.; Egidi, F.; Goings, J.; Peng, B.; Petrone, A.; Henderson, T.; Ranasinghe, D.; Zakrzewski, V. G.; Gao, J.; Rega, N.; Zheng, G.; Liang, W.; Hada, M.; Ehara, M.; Toyota, K.; Fukuda, R.; Hasegawa, J.; Ishida, M.; Nakajima, T.; Honda, Y.; Kitao, O.; Nakai, H.; Vreven, T.; Throssell, K.; Montgomery Jr., J. A.; Peralta, J. E.; Ogliaro, F.; Bearpark, M. J.; Heyd, J. J.; Brothers, E. N.; Kudin, K. N.; Staroverov, V. N.; Keith, T. A.; Kobayashi, R.; Normand, J.; Raghavachari, K.; Rendell, A. P.; Burant, J. C.; Iyengar, S. S.; Tomasi, J.; Cossi, M.; Millam, J. M.; Klene, M.; Adamo, C.; Cammi, R.; Ochterski, J. W.; Martin, R. L.; Morokuma, K.; Farkas, O.; Foresman, J. B.; Fox, D. J. Gaussian 16 Rev. A.03, 2016.

(2) Becke, A. D. Density-Functional Exchange-Energy Approximation with Correct Asymptotic Behavior. *Phys. Rev. A* **1988**, *38* (6), 3098–3100. https://doi.org/10.1103/PhysRevA.38.3098.

(3) Perdew, J. P. Generalized Gradient Approximation Made Simple. *Phys. Rev. Lett.* **1996**, *77* (18), 3865–3868. https://doi.org/10.1103/PhysRevLett.77.3865.

(4) Grimme, S.; Antony, J.; Ehrlich, S.; Krieg, H. A Consistent and Accurate Ab Initio Parametrization of Density Functional Dispersion Correction (DFT-D) for the 94 Elements H-Pu. *J. Chem. Phys.* **2010**, *132* (15), 154104. https://doi.org/10.1063/1.3382344.

(5) Solis, B. H.; Maher, A. G.; Honda, T.; Powers, D. C.; Nocera, D. G.; Hammes-Schiffer, S. Theoretical Analysis of Cobalt Hangman Porphyrins: Ligand Dearomatization and Mechanistic Implications for Hydrogen Evolution. *ACS Catal.* **2014**, *4* (12), 4516–4526. https://doi.org/10.1021/cs501454y.

(6) Wang, Y.-H.; Schneider, P. E.; Goldsmith, Z. K.; Mondal, B.; Hammes-Schiffer, S.; Stahl, S. S. Brønsted Acid Scaling Relationships Enable Control Over Product Selectivity from O2 Reduction with a Mononuclear Cobalt Porphyrin Catalyst. *ACS Cent. Sci.* **2019**, *5* (6), 1024–1034. https://doi.org/10.1021/acscentsci.9b00194.

(7) Rooney, C. L.; Lyons, M.; Wu, Y.; Hu, G.; Wang, M.; Choi, C.; Gao, Y.; Chang, C.-W.; Brudvig, G. W.; Feng, Z.; Wang, H. Active Sites of Cobalt Phthalocyanine in Electrocatalytic CO2 Reduction to Methanol. *Angew. Chem. Int. Ed.* **2024**, *63* (2), e202310623. https://doi.org/10.1002/anie.202310623.

(8) Hay, P. J.; Wadt, W. R. Ab Initio Effective Core Potentials for Molecular Calculations. Potentials for the Transition Metal Atoms Sc to Hg. *J. Chem. Phys.* **1985**, *82* (1), 270–283. https://doi.org/10.1063/1.448799.

(9) Hay, P. J.; Wadt, W. R. Ab Initio Effective Core Potentials for Molecular Calculations. Potentials for K to Au Including the Outermost Core Orbitals. *J. Chem. Phys.* **1985**, *82* (1), 299–310. https://doi.org/10.1063/1.448975.

(10) Wadt, W. R.; Hay, P. J. Ab Initio Effective Core Potentials for Molecular Calculations. Potentials for Main Group Elements Na to Bi. *J. Chem. Phys.* **1985**, *82* (1), 284–298. https://doi.org/10.1063/1.448800.

(11) Ditchfield, R.; Hehre, W. J.; Pople, J. A. Self-Consistent Molecular-Orbital Methods. IX. An Extended Gaussian-Type Basis for Molecular-Orbital Studies of Organic Molecules. *J. Chem. Phys.* **1971**, *54* (2), 724–728. https://doi.org/10.1063/1.1674902.

(12) Francl, M. M.; Pietro, W. J.; Hehre, W. J.; Binkley, J. S.; Gordon, M. S.; DeFrees, D. J.; Pople, J. A. Self-consistent Molecular Orbital Methods. XXIII. A Polarization-type Basis Set for Second-row Elements. *J. Chem. Phys.* **1982**, *77* (7), 3654–3665. https://doi.org/10.1063/1.444267.

(13) Hehre, W. J.; Ditchfield, R.; Pople, J. A. Self—Consistent Molecular Orbital Methods. XII. Further Extensions of Gaussian—Type Basis Sets for Use in Molecular Orbital Studies of Organic Molecules. *J. Chem. Phys.* **1972**, *56* (5), 2257–2261. https://doi.org/10.1063/1.1677527.

(14) Barone, V.; Cossi, M. Quantum Calculation of Molecular Energies and Energy Gradients in Solution by a Conductor Solvent Model. *J. Phys. Chem. A* **1998**, *102* (11), 1995–2001. https://doi.org/10.1021/jp9716997.

(15) Cossi, M.; Rega, N.; Scalmani, G.; Barone, V. Energies, Structures, and Electronic Properties of Molecules in Solution with the C-PCM Solvation Model. *J. Comput. Chem.* **2003**, *24* (6), 669–681. https://doi.org/10.1002/jcc.10189.

(16) Rappe, A. K.; Casewit, C. J.; Colwell, K. S.; Goddard, W. A. I.; Skiff, W. M. UFF, a Full Periodic Table Force Field for Molecular Mechanics and Molecular Dynamics Simulations. *J. Am. Chem. Soc.* **1992**, *114* (25), 10024–10035. https://doi.org/10.1021/ja00051a040.

(17) Hutchison, P.; Smith, L. E.; Rooney, C. L.; Wang, H.; Hammes-Schiffer, S. Proton-Coupled Electron Transfer Mechanisms for CO2 Reduction to Methanol Catalyzed by Surface-Immobilized Cobalt Phthalocyanine. *J. Am. Chem. Soc.* **2024**, *146* (29), 20230–20240. https://doi.org/10.1021/jacs.4c05444.

(18) Stephens, P. J.; Devlin, F. J.; Chabalowski, C. F.; Frisch, M. J. Ab Initio Calculation of Vibrational Absorption and Circular Dichroism Spectra Using Density Functional Force Fields. *J. Phys. Chem.* **1994**, *98* (45), 11623–11627. https://doi.org/10.1021/j100096a001.

(19) Becke, A. D. Density-functional Thermochemistry. III. The Role of Exact Exchange. *J. Chem. Phys.* **1993**, *98* (7), 5648–5652. https://doi.org/10.1063/1.464913.

(20) Lee, C. Development of the Colle-Salvetti Correlation-Energy Formula into a Functional of the Electron Density. *Phys. Rev. B* **1988**, *37* (2), 785–789. https://doi.org/10.1103/PhysRevB.37.785.

(21) Vosko, S. H.; Wilk, L.; Nusair, M. Accurate Spin-Dependent Electron Liquid Correlation Energies for Local Spin Density Calculations: A Critical Analysis. *Can. J. Phys.* **1980**, *58* (8), 1200–1211. https://doi.org/10.1139/p80-159.

(22) Zhao, Y.; Truhlar, D. G. A New Local Density Functional for Main-Group Thermochemistry, Transition Metal Bonding, Thermochemical Kinetics, and Noncovalent Interactions. *J. Chem. Phys.* **2006**, *125* (19), 194101. https://doi.org/10.1063/1.2370993.

(23) Bondi, A. Van Der Waals Volumes and Radii. *J. Phys. Chem.* **1964**, *68* (3), 441–451. https://doi.org/10.1021/j100785a001.

(24) Marenich, A. V.; Cramer, C. J.; Truhlar, D. G. Universal Solvation Model Based on Solute Electron Density and on a Continuum Model of the Solvent Defined by the Bulk Dielectric Constant and Atomic Surface Tensions. *J. Phys. Chem. B* **2009**, *113* (18), 6378–6396. https://doi.org/10.1021/jp810292n.

(25) Laidler, K. J.; King, M. C. Development of Transition-State Theory. *J. Phys. Chem.* **1983**, *87* (15), 2657–2664. https://doi.org/10.1021/j100238a002.

(26) Kresge, A. J. The Brønsted Relation – Recent Developments. *Chem. Soc. Rev.* **1973**, *2* (4), 475–503. https://doi.org/10.1039/CS9730200475.

(27) Evans, M. G.; Polanyi, M. Inertia and Driving Force of Chemical Reactions. *Trans. Faraday Soc.* **1938**, *34* (0), 11–24. https://doi.org/10.1039/TF9383400011.

(28) Evans, M. G.; Polanyi, M. Some Applications of the Transition State Method to the Calculation of Reaction Velocities, Especially in Solution. *Trans. Faraday Soc.* **1935**, *31* (0), 875–894. https://doi.org/10.1039/TF9353100875.

(29) Eyring, Henry. The Activated Complex and the Absolute Rate of Chemical Reactions. *Chem. Rev.* **1935**, *17* (1), 65–77. https://doi.org/10.1021/cr60056a006.

(30) Bronsted, J. N. Acid and Basic Catalysis. *Chem. Rev.* **1928**, *5* (3), 231–338. https://doi.org/10.1021/cr60019a001.

(31) Rountree, E. S.; McCarthy, B. D.; Eisenhart, T. T.; Dempsey, J. L. Evaluation of Homogeneous Electrocatalysts by Cyclic Voltammetry. *Inorg. Chem.* **2014**, *53* (19), 9983–10002. https://doi.org/10.1021/ic500658x.

(32) Costentin, C.; Savéant, J.-M. Multielectron, Multistep Molecular Catalysis of Electrochemical Reactions: Benchmarking of Homogeneous Catalysts. *ChemElectroChem* **2014**, *1* (7), 1226–1236. https://doi.org/10.1002/celc.201300263.